Copyright Undertaking

ROBUST ROOM-TEMPERATURE FERROELECTRIC ULTRATHIN CHALCOGENIDE LAYERS AND VAN DER WAALS HETEROSTRUCTURES

IO Weng Fu

MPhil
The Hong Kong Polytechnic University
2021

The Hong Kong Polytechnic University
Department of Applied Physics

Robust Room-Temperature Ferroelectric Ultrathin Chalcogenide Layers and van der Waals Heterostructures

IO Weng Fu

A thesis submitted in partial fulfillment of the requirements for
the degree of Master of Philosophy

August 2020

CERTIFICATE OF ORIGINALITY

I hereby declare that this thesis is my own work and that, to the best of my knowledge and belief, it reproduces no material previously published or written, nor material that has been accepted for the award of any other degree or diploma, except where due acknowledgement has been made in the text.

____(Signed)

___________IO Weng Fu__________(Name of student)

Abstract

Emerging two-dimensional (2D) ferroelectric materials with unique structures and extraordinary electrical properties have drawn enormous research attention for the applications in nanoelectronic and optoelectronic devices. In traditional ferroelectrics, their potential nanoscale electronic applications are seriously hindered by the size effect. With the merit of van der Waals (vdW) stacking layer structure, 2D materials without the restriction of the fundamental size effect are promising to overcome the increasing effect of depolarization field in ultrathin ferroelectric materials, therefore opening up a new route for exploring ferroelectric phenomena at low dimensionality. Although various potential 2D layered ferroelectric materials have been predicted with theoretical calculations, plenty of them still requires to be implemented with experimental works. To date, experimental achievements of ultrathin layered ferroelectrics are still very limited, and further investigations are urgently needed.

In this thesis, the robust high-temperature 2D out-of-plane ferroelectricity of α-In_2Se_3 nanoflakes with the existence of switchable electric polarization above 200 °C is demonstrated. First, high-quality single-crystallized α-In_2Se_3 nanosheets were fabricated via chemical vapor deposition (CVD), and their phase and crystal quality were examined using optical microscopy and Raman spectroscopy. The non-centrosymmetric structure of the as-grown α-In_2Se_3 samples was evident under second harmonic generation (SHG) microscopy. The crystal structure and chemical composition of α-In_2Se_3 were studied by X-ray photoelectron spectroscopy (XPS) and transmission electron microscopy (TEM), and the morphology was determined with atomic force microscopy (AFM). The ferroelectric properties were investigated on α-In_2Se_3/Pt heterostructure at different temperatures using piezoresponse force microscopy (PFM) equipped with a polyheater. Distinctive polarization switching and ferroelectric domains are observable in ultrathin α-In_2Se_3 films down to 10 nm in a wide range of temperatures. The coercive field causing polarization reversal in 2D α-In_2Se_3 demonstrates a thickness dependency at room temperature and increases significantly when reducing the film thickness. When the temperature of samples varies, there shows no obvious changes in the value of coercive voltage for α-In_2Se_3 nanosheets with identical thickness. The overall results effectively verify the high stability of ferroelectric phenomena in CVD-grown α-In_2Se_3 nanoflakes at high temperature reaching above 200 °C and provide critical insights for 2D materials to apply in next-generation high-temperature nanoelectronic devices.

On the other hand, we demonstrate the out-of-plane ultrathin ferroelectricity in two vdW layered transition metal thiophosphates: $CuInP_2S_6$ (CIPS) and $CuCrP_2S_6$ (CCPS), both possessing critical temperatures above room temperature and are not comprehensively investigated with experiments. The crystal structure and phase of CIPS and CCPS crystal were studied by Raman spectroscopy, X-ray diffraction (XRD) and TEM, and their broken inverse symmetry was verified using second harmonic imaging microscopy (SHIM). The ferroelectric phenomena at room temperature were characterized by PFM. In experiment, we discover stable out-of-plane ferroelectricity in 2D CIPS and CCPS samples at different thicknesses, in which switchable spontaneous polarization field and butterfly-shaped amplitude signals are observed in CIPS and CCPS nanoflakes down to 9 nm and 6 nm, respectively. Furthermore, the origin of 2D ferroelectricity in CIPS and CCPS is discussed.

In summary, the outstanding thermal stability of ferroelectricity in CVD-grown α-In_2Se_3 nanosheets is verified in this thesis with desirable ferroelectric properties. Also, robust room-temperature ferroelectric phenomena are observed in ultrathin CIPS and CCPS thin films with a thickness of less than 10 nm. It is believed our work presented in this thesis broadens the 2D ferroelectric family that accomplished with experiments and facilitates the potential 2D layered ferroelectric materials in nanoelectronic applications.

List of Publications

1. **Weng Fu Io**, Shuoguo Yuan, Sin Yi Pang, Lok Wing Wong, Jiong Zhao, and Jianhua Hao*. “Temperature-and thickness-dependence of robust out-of-plane ferroelectricity in CVD grown ultrathin van der Waals α-In_2Se_3 layers”, ***Nano Res.*** 2020, 13, 7, 1897–1902.
2. Yongxin Lyu, Zehan Wu, **Weng Fu Io** and Jianhua Hao*, “Observation and theoretical analysis of near-infrared luminescence from CVD grown lanthanide Er doped monolayer MoS_2 triangles”, ***Appl. Phys. Lett.*** 2019, 115, 153105.
3. Sin Yi Pang, **Weng Fu Io**, Lok Wing Wong, Jiong Zhao, and Jianhua Hao*, “Efficient energy conversion and storage based on robust fluoride-free self-assembled 1d niobium carbide in 3d nanowire network”, ***Adv. Sci.*** 2020, 7, 10, 1903680.
4. Ran Ding, Chun-Ki Liu, Zehan Wu, Feng Guo, Sin-Yi Pang, Lok Wing Wong, **Weng Fu Io,** Shuoguo Yuan, Man-Chung Wong, Michal Bartlomiej Jedrzejczyk, Jiong Zhao, Feng Yan, and Jianhua Hao*, “A general wet transferring approach for diffusion-facilitated space-confined grown perovskite single-crystalline optoelectronic thin films”, ***Nano Lett.*** 2020, 20, 4, 2747-2755.

5. Feng Guo, Yongxin Lyu, Michal Bartlomiej Jedrzejczyk, Yuqian Zhao, **Weng Fu Io**, Gongxun Bai, Wenzhuo Wu, and Jianhua Hao*, "Piezoelectric biaxial strain effects on the optical and photoluminescence spectra of 2D III-VI compound α-In_2Se_3 nanosheets", ***Appl. Phys. Lett.*** 2020, 116, 113101.

6. Shuoguo Yuan, **Weng Fu Io**, Jianfeng Mao, Yancong Chen, Xin Luo, and Jianhua Hao*, "Enhanced piezoelectric response of layered In_2Se_3/MoS_2 nanosheet-based van der Waals heterostructures", ***ACS Appl. Nano Mater.*** 2020.

Acknowledgements

First and foremost, I would like to express my sincere gratitude to my supervisor, Prof. Jianhua Hao, for his patient guidance and supervision in my two years of MPhil study. His profound insights and passionate attitude towards research influenced and encouraged me a lot throughout my entire postgraduate study. He not only gave inspiring advices and valuable assistance in research, but also provided sufficient care and support in my daily life.

I sincerely appreciate Dr. Vincent Chan, Dr. Hardy Lui and Dr. Terence Wong for their assistance in equipment utilization for my research works.

I would also like to express my thankfulness to my research groupmates Ms. Sin Yi Pang, Ms. Yongxin Lyu, Mr. Shuoguo Yuan, Dr. Ran Ding, Mr. Zehan Wu, Ms. Yuqian Zhao, Dr. Man-Chung Wong, Mr. Feng Guo, Mr. Menglin Song, Mr. Jianfeng Mao, Mr. Jedrzejczyk Michal Bartlomiej, and Dr. Beining Zheng for their great support and encouragement, and for the friendship we established in this two years.

I acknowledge the financial support from Research Grants Council of Hong Kong (GRF No. PolyU 153033/17P).

At last, I would like to express my deepest thanks to my family members for their continuous support, endless love and understanding in my two years of postgraduate study in PolyU. I am also grateful to my friends who accompanied me all the way in this journey.

Table of Contents

List of Figures

List of Tables

Chapter 1 Introduction

1.1 Background of two-dimensional van der Waals layered materials

The first discovery of single-layer graphite, which known as graphene, has triggered immense research interests on atomic-scale two-dimensional (2D) materials for more than one decade [1]. Atomically thin layered materials exist several unprecedented properties that do not appear in their bulk counterparts, and the emergence of ultrathin layered materials opens up new opportunities in the conventional semiconducting industry and multifunctional electronic device applications. As the earliest and most extensively studied van der Waals (vdW) layered 2D materials, graphene is shown to possess various outstanding electrical, mechanical and optical characteristics such as excellent thermal conductivities (~4400-5800 W/mK) [1], ultrahigh room temperature carrier mobility (10,000 $cm^2/V·s$), very large theoretical surface area (2630 m^2/g), ultrahigh Young's modulus (~1 TPa), and high optical transparency (97.7%), beneficial for applications in field-effect transistors (FET), high-performance energy storage devices, flexible solar cells, and as transparent conducting material in photonic devices [1-8]. The research on graphene has been growing dramatically since 2004 and thousands of graphene-related works are published every year. Indeed, pristine graphene has been comprehensively investigated and is commercially utilized in our daily life with continuously improved quality.

Inspired by the extraordinary properties of graphene, researchers began to pay attention to exploring other 2D materials with similar vdW layered structure which exhibit versatile material characteristics, such as transition metal dichalcogenides (TMDs, e.g. MoS_2, $MoSe_2$, $MoTe_2$, WS_2, WTe_2) [9-13], metal oxides [14-16] and layered double hydroxides (LDHs) [17, 18]. Moreover, other categories of atomically thin 2D materials such as black phosphorus (BP) [19-21], MXenes (e.g. $TiCT_x$, V_2CT_x) [22, 23], elemental metals [24], metal organic frameworks (MOFs) [25, 26] and covalent organic frameworks (COFs) [27, 28] are explored and studied in recent years (Figure 1.1). Along with the rapid exploration of 2D nanomaterials, many different synthesis methods including mechanical exfoliation, chemical vapor deposition (CVD), molecular beam epitaxy (MBE), pulsed laser deposition (PLD) and electrochemical-etching (E-etching) are developed to prepare high-quality ultrathin 2D materials [22, 29, 30]. Intriguingly, other 2D layered materials include several essential categories of materials such as conductors, semiconductors and insulators with different bandgaps and they illustrate excellent performances in different functional fields. With various unique physical, optical, and electrical features, ultrathin 2D materials are potential candidates for applications such as electronics, optoelectronics, catalysis, biomedicines, sensing devices, and energy harvesting and storage devices [31].

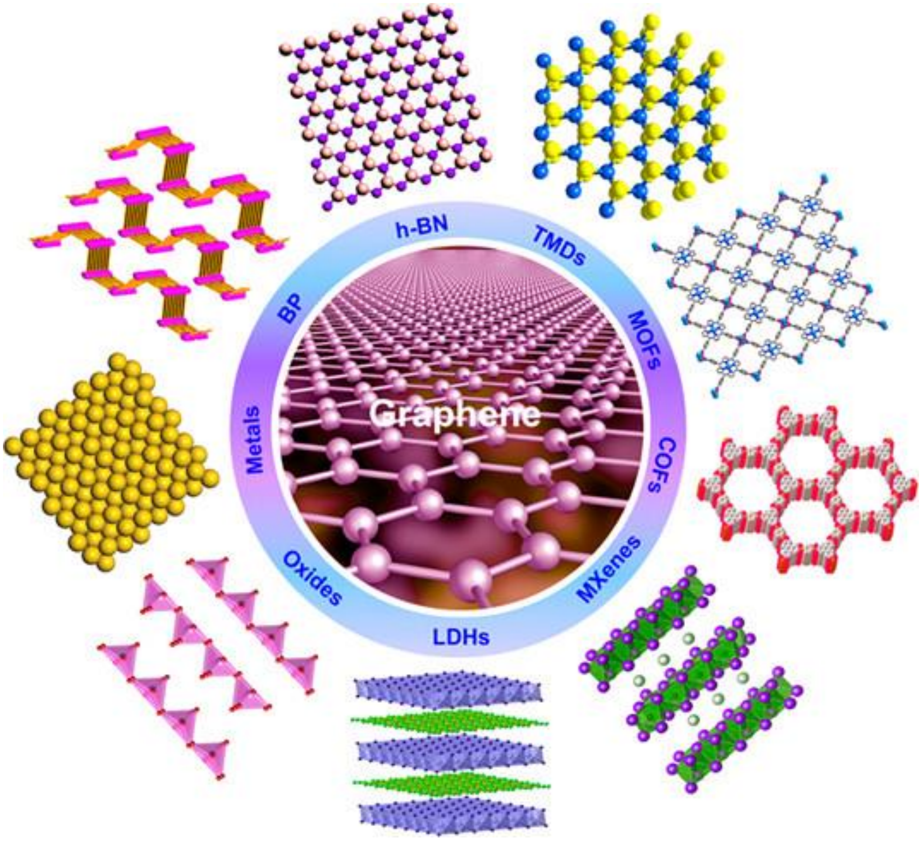

Figure 1.1 Schematic diagrams of different types of ultrathin 2D materials. [32]

1.2 Assembly of van der Waals heterostructures

The atoms in a single layer of vdW nanomaterials are held together by strong ionic and/or covalent bonds and the neighboring layers are linked via weak electrostatic (vdW) forces. As the surface atoms of ultrathin vdW layered materials are completely saturated, they possess high surface areas with dangling bond-free surfaces, enabling the possibility to achieve atomic-scale heterogeneous junctions between distinct materials via weak interplanar vdW interactions [33-35]. Indeed, vdW interactions are not only limited to the stacking between layered materials, but also between any passivated and dangling-bond-free surfaces. Therefore, a variety of hybrid structures can be constructed with novel properties, multifunctionalities and enhanced performances without the necessity of matching the crystal lattices of materials, which is not feasible in other types of materials.

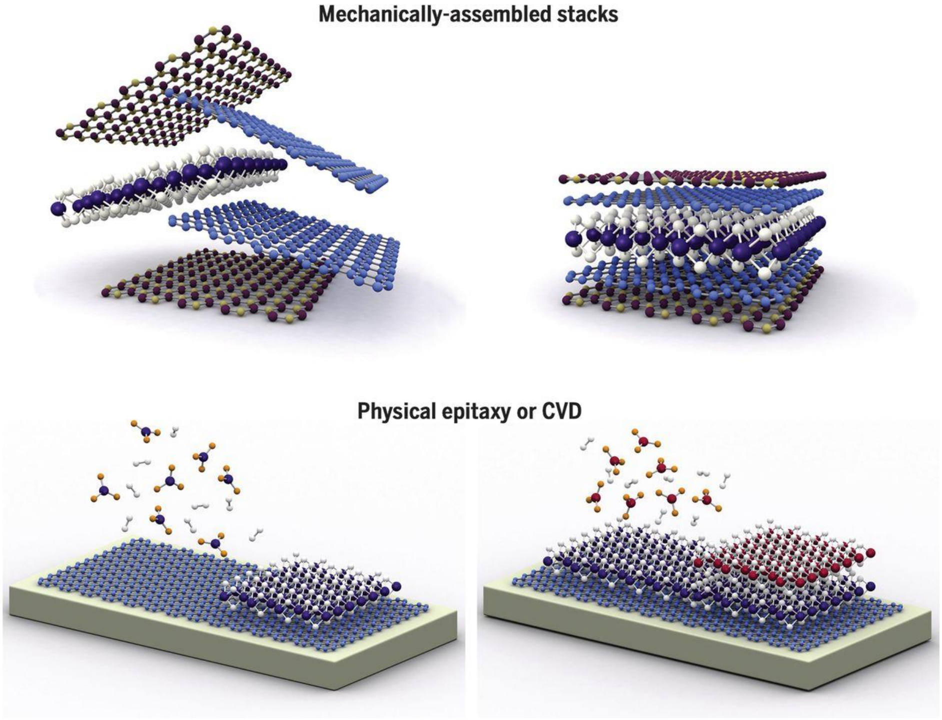

Figure 1.2 Fabrication of vdW heterostructures. Mechanical assembly method (top) and large-scale heterostructure growth by CVD or physical epitaxy (bottom). [33]

Over the past decade, the research on vertically stacked vdW heterostructures has grown rapidly and many fascinating phenomena such as superconductivity, topological insulator and valleytronics are reported in various constructed heterostructures that are previously not available [33, 35]. Similar to the fabrication of 2D nanomaterials, the heterostructures can be constructed through both top-down and bottom-up approaches, as shown in Figure 1.2.

Currently, the most promising strategy to create heterostructures is the micromechanical transfer technique [36-38]. This approach arises from the fabrication of graphene devices on hexagonal boron nitride (h-BN) substrates with improved performance than that on standard SiO_2 substrates by Dean *et al.* in 2010 [39]. The first step of this method is to prepare a dangling-bond-free 2D material onto an arbitrary substrate by mechanical exfoliation or other synthetic methods. Then the next layered material can be vertically stacked onto the first material by dry and/or wet transfer techniques with the assistance of polymers such as polydimethylsiloxane (PDMS), polypropylene carbonate (PPC), polyvinyl acetate (PVA) and polymethyl methacrylate (PMMA). The transfer process is usually carried out with the help of microscope equipped with micromanipulators that is essential for accurate alignment of nanoflakes. In a typical PMMA-assisted wet-transfer process, a layer of PMMA is coated onto the target 2D material and immersed in water. The water molecules are intercalated between the hydrophilic substrate and the hydrophobic PMMA film carrying the target 2D material and delaminate the polymer film from the substrate. Then the PMMA film with 2D material is transferred onto another desired material/substrate to form a vdW heterostructure and the PMMA layer is directly dissolved in acetone solution. The main advantage of the mechanical transfer method to create heterostructures is its high versatility and flexibility, as long as the transferred materials are sufficiently stable and robust during the whole transfer and restack process. It also offers a relatively simple route to obtain vdW heterostructures with atomically sharp and thin interfaces.

However, the top-down physical transfer approach is intrinsically not practical in mass production of vdW heterostructures. While the alternative bottom-up approach through chemical techniques such as CVD and MBE can directly deposit the heterostructures and therefore potentially enable large-scale fabrication of vdW heterostructures with high controllability. Via CVD technique, several types of heterostructures are created based on the as-grown ultrathin layered materials such as graphene, BN and TMDs (e.g. MoS_2, WSe_2 etc.) [40-43], on top of other materials. For instance, Gong et.al demonstrate [42] a one-step fabrication strategy to grow high-quality vertically stacked and in-plane interconnected WS_2/MoS_2 heterostructures, and the methodology and morphology of monolayer WS_2/MoS_2 heterostructures are displayed in Figure 1.3. In addition, He and his co-workers present a two-step CVD method to subsequently deposit two different ultrathin materials, forming ultrathin $In_2Se_3/MoSe_2$ heterostructures with efficient charge transfer properties. Although large-scale vdW heterostructures can be realized through the bottom-up approach, matching the highly sensitive growing conditions of different 2D nanomaterials and at the same time maintaining high crystal qualities is still challenging, therefore limiting the current available synthesized vdW heterostructures.

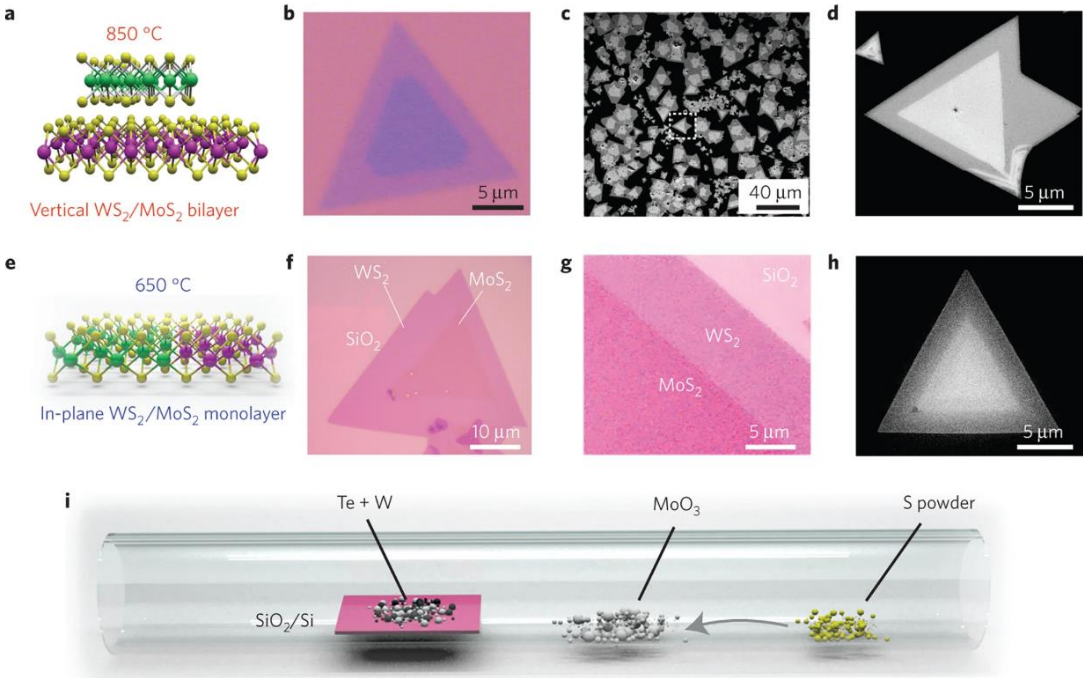

Figure 1.3 Schematic illustration of the morphologies and synthesis process of the vertically stacked and in-plane WS_2/MoS_2 heterostructures. (a)-(d) Schematic, optical and SEM images of the vertical WS_2/MoS_2 heterostructures, and (e)–(h) that of the WS_2/MoS_2 in-plane heterojunctions. (i) Schematic diagram of the CVD synthesis for both vertical and in-plane heterostructures. [42]

1.3 Ultrathin ferroelectric films

1.3.1 Traditional perovskite ferroelectric materials

Ferroelectric is a type of functional material that possesses at least two equilibrium directions of spontaneous electric polarization at zero bias, and the polarization orientations are switchable when an external electric field is applied. Generally, the ferroelectric properties in ferroelectric materials vanish at Curie temperature (T_c) with the structural transformation from nonsymmetric ferroelectric phase into the paraelectric phase with higher symmetry. In bulk ferroelectric crystals, the ferroelectric properties are usually characterized macroscopically by hysteresis loop observable in the polarization–electric field (P–E) analysis as shown in Figure 1.4. Ferroelectrics is a sub-family of dielectric materials, and all ferroelectrics innately exist dielectric, piezoelectric, and pyroelectric features in addition to ferroelectric features, which are essential in a broad diversity of applications such as optoelectronics, catalysis, sensors, transistors, capacitors, transducers, actuators, artificial synapses and nonvolatile memory devices [44-47].

The research on ferroelectrics started early from the demonstration of ferroelectricity in Rochelle salt by Valasek [48] in the last century. Followed by the discovery of ferroelectric Rochelle salt, various ferroelectric crystals are extensively studied over the last decades. Traditional ferroelectric perovskite oxides are the most widely studied ferroelectrics with a general structure of ABO_3, where A can be alkali, alkaline earth and rare earth such as Ba^{2+}, Sr^{2+} and Pb^{2+} and B can be 3d, 4d and 5d transition metal ions [49, 50]. The ferroelectric phase of the ferroelectric perovskites is formed through the structural transformation from the high-symmetric paraelectric cubic phase to the nonsymmetric ferroelectric phase below curie temperature. Accompanied by the paraelectric–ferroelectric phase transition, the A cations are displaced with respect to the B anions, generating stable electric dipoles in the unit cells which do not coincide and originate the spontaneous polarization in the ferroelectric perovskite oxides.

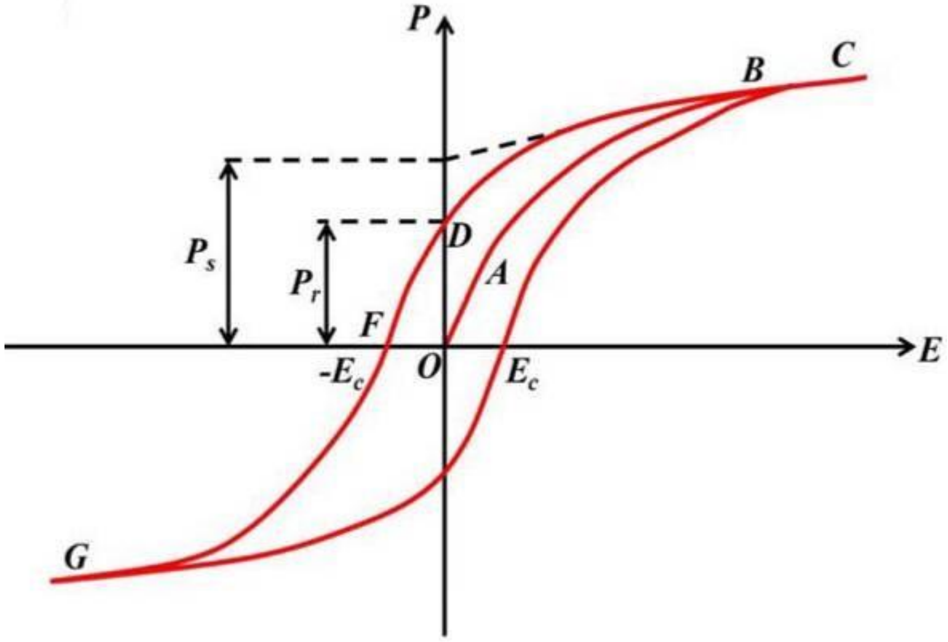

Figure 1.4 P-E hysteresis loop for typical ferroelectric materials. [51]

1.3.2 Size effect in traditional ferroelectric perovskite thin films

The typical family of perovskite-type ferroelectric films includes $BaTiO_3$ (BTO), $PbTiO_3$ (PTO), $BiFeO_3$ (BFO) and $Pb[Zr_xTi_{1-x}]O_3$ (PZT) , and they are widely utilized in practical devices such as photovoltaic devices, memory devices, pyroelectric and piezoelectric microsensors and actuators [44, 52-54]. Owing to the trend in miniaturization and integration of electronic devices and fast technological development, ultrathin ferroelectric materials have drawn substantial attention in recent years. The demand for technological advances revealed the intrinsic size effect in conventional ferroelectrics [55, 56]. The polarization field in ferroelectrics is originated from the non-centrosymmetric structure of the crystal forming electric dipole moments in the materials. Because of the cooperative behaviors of dipoles and the charges accumulated on the material interfaces being uncompensated which generate an internal depolarization field perpendicular to the surface, ferroelectricity in ferroelectric perovskite oxides were believed to disappear below a certain critical size of about tens of nanometers with poor complementary metal-oxide-semiconductor (CMOS) compatibility [57, 58].

Until 2000s, enormous efforts have been made to overcome the effect of the depolarization field in perovskite ferroelectrics and remarkable advancements were achieved in the fabrication techniques of thin films. Several traditional oxide ferroelectrics are reported to maintain ferroelectric properties in atomically thin layers. In 2003, Junquera and Ghosez [55] demonstrated the possibility of retaining ferroelectricity in BTO down to 2.4 nm with $SrRuO_3$ electrodes by first-principles calculations. In 2004, Fong and his colleagues [59] successfully deposit epitaxial PTO films on insulating $SrTiO_3$ substrates which exhibit stable room-temperature ferroelectricity with thickness down to 1.2 nm. The selected substrates are lattice-matched to the ferroelectric PTO films, and the films only polarize in out-of-plane direction due to compressive strain. In 2005, Sai and his co-workers [56] showed that the critical thickness of PTO can be lowered down to less than 10 Å with the use of Pt electrodes through density functional theory (DFT) calculations. This is due to the effect of metallic screening and electrode-ferroelectrics interfaces. Sai's group also found that BTO does not show similar result as PTO with the same electrode material, as the work functions of the two ferroelectric materials are different which possibly affect their ferroelectric behavior in ultrathin films as well. In the following year, Gerra *et al.* [60] verified with DFT calculations that BTO films can sustain a stable ferroelectric phase at room temperature down to 1.2 nm using $SrRuO_3$ as electrodes. Nonetheless, maintaining the ferroelectric effects in ultrathin perovskite oxide films is still challenging which requires the cooperation of specific electrodes and/or careful selection of substrates with small lattice mismatch to that of the ferroelectric materials, inhibiting the possible development of interface-assembling heterostructures and limiting their potential in electronic applications electronics towards miniaturization. Also, the introduction of defects such as oxygen vacancies and dangling bonds in the ferroelectric films during high-temperature deposition and device fabrication process are usually unavoidable, and potentially degrading the ferroelectric performances of the films [61, 62].

1.3.3 2D ferroelectric materials

Besides the traditional ferroelectric perovskite oxides, simple binary oxides (Hf/ ZrO_2) system have received considerable attention recently which shows the tuning of intrinsic properties with the existence of stable ferroelectricity/antiferroelectricity upon doping elements such as Si, Zr, Ga, Al, Sr and La [63-65]. Bulk HfO_2 crystal exists several phases upon different temperature, pressure and stress including monoclinic $P2_1/c$ (m-phase), tetragonal $P4_2/nmc$ (t-phase), orthorhombic $Pbca$ and $Pnma$ phases (o-phase). All the polymorphs of HfO_2 are symmetric and are excluded the presence of ferroelectricity. In 2011, ferroelectricity was first discovered in Si-doped HfO_2 thin films of ~10 nm thick, with less than 4% of Si dopant concentration [66]. In 2020, stable out-of-plane ferroelectricity was successfully found in $Hf_{0.8}Zr_{0.2}O_2$ (HZO) nanosheets down to the thickness of only 1 nm, fabricated by low-temperature atomic layer deposition (ALD) [67]. In the nanoscale ferroelectrics, P–E hysteresis analysis is not suitable for characterizing the intrinsic ferroelectric responses since leakage current can cause false signals in ultrathin materials. Instead, piezoelectric force microscopy (PFM) is employed to observe the ferroelectric responses in nanomaterials and the PFM measurements of the HZO nanosheets are shown in Figure 1.5. Moreover, the polar distortions in HZO system are enhanced as the film thickness decreases, resulting in the enhancement of ferroelectricity in ultrathin HZO films which opposite to that in the typical perovskite ferroelectrics.

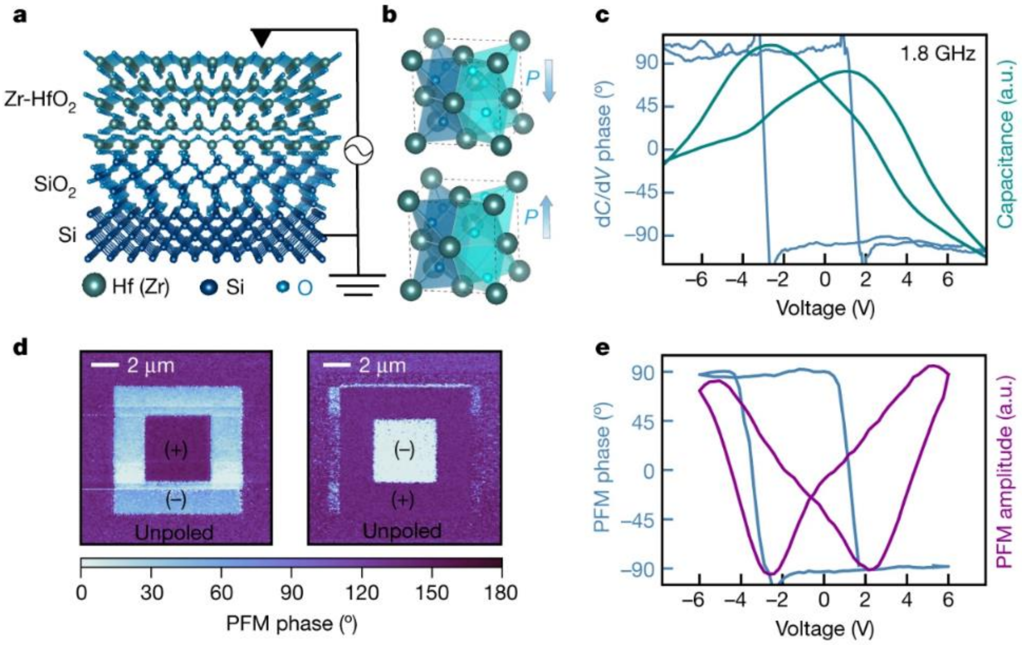

Figure 1.5 (a) Schematic diagrams of the HZO /SiO_2 heterostructure and (b) the ferroelectric HZO unit cell with two different the polarization directions. (c) Microwave-frequency canning capacitance microscopy for a ten-cycle HZO film presenting butterfly-shaped loop in C–V

curve and verifying ferroelectricity in 1nm thick HZO film. (d) PFM phase images of rewritten polarization states on ultrathin HZO film.(e) Phase and amplitude switching spectroscopy showing butterfly-shaped amplitude and phase hysteresis loop with switching of 180°. [67]

On the other hand, after the investigation of the first 2D monolayer material graphene, a large amount of research works is conducted to search for potential ultrathin ferroelectric materials with varying structures than the typical ferroelectric perovskite oxides. Significant progress is made in different aspects including the thin films synthesis, property characterizations and ferroelectric device designs [46, 68]. Several non-traditional ultrathin vdW layered ferroelectric materials are predicted theoretically and proved experimentally the existence of ferroelectricity. In comparison to the traditional ferroelectric oxides and Hf/ZrO_2-based systems, 2D vdW materials hold the merits of atomically thin and flexible structure, dangling-bond free surfaces, no constraints of lattice mismatch, high carrier mobility, high compatibility with other materials, and especially the possibility of constructing vdW heterostructures with no restriction in the matching of lattices [61, 62, 68-70]. In the past several years, the possibility of intrinsic ferroelectricity in 2D layered materials has been sufficiently verified by theoretical predictions such as in single-layer group IV chalcogenides (SnS, SnSe, GeS and GeSe) [71], elemental group V monolayers [72], distorted 1*T*-phase

TMDs [11, 73], transition metal thiophosphate ($AgBiP_2Se_6$, $CuInP_2S_6$, etc) [74, 75] and III_2–V_3 compounds (In2Se3) [76], and many of them retain robust ferroelectricity at room temperature in atomically thin thickness. In ultrathin materials, ferroelectricity can be categorized based on the polarization field directions along in-plane (direction parallel to surface) and out--of-plane (direction perpendicular to surface) ferroelectricity. To date, stable room temperature in-plane ferroelectricity is experimentally observed in SnTe, β′-In_2Se_3, SnS and BA_2PbCl_4 thin films [77-80]. For example, as reported in literature, ferroelectricity can still be observed one unit-cell thick SnTe films at ~270 K, and ferroelectricity can be maintained at room temperature in 2-4 unit-cell thick SnTe films [77]. The high stability of the in-plane ferroelectricity can be attributed to the 180° alternating polarization domain stripes formed in ultrathin SnTe films. In addition, Zheng *et.al* [78] reported in 2018 with the in-plane ferroelectricity in exfoliated β′-In_2Se_3 with thickness down to 45 nm, which was long believed to be a metastable polymorph of In_2Se_3. 2D layered materials with in-plane ferroelectricity can sustain their ferroelectric properties in ultrathin limit and need not overcome the perturbations of out-of-plane depolarization field. However, the in-plane spontaneous polarization direction also largely restricting their potentials in device applications. Besides, out-of-plane spontaneous polarization is observed with experiments in nanoscale thin films such as WTe_2, $CuInP_2S_6$ and distorted 1*T*-$MoTe_2$

[81-83], and intercorrelated ferroelectricity is demonstrated in α-In_2Se_3. Their ferroelectricity originates from different intrinsic mechanisms. Comparatively, the out-of-plane ferroelectricity is more advantageous in designing nanoscale devices, but the polarization strength usually declines with thinner layers due to the effect of the depolarization field.

Table 1.1 A summary of the critical thickness and polarization value of the experimentally reported 2D vdW ferroelectric materials.

Materials	**Dipole direction**	**Critical thickness (nm)**	**Polarization value (μC/cm^2)**	**Ref.**
SnTe	In-Plane	0.63	—	[77]
SnS	In-Plane	0.58	26	[71, 80]
β′-In_2Se_3	In-Plane	45	—	[78]
BA_2PbCl_4	In-Plane	1.7	4	[79]
*d*1*T*-$MoTe_2$	Out-of-plane	0.8	—	[83]
WTe_2	Out-of-plane	1.4	—	[82]
α-In_2Se_3	In-plane and out-of-plane	2H: 1.2 3R: 3	—	[84, 85]
$CuInP_2S_6$	Out-of-plane	4	4	[86]
$CuCrP_2S_6$	Out-of-plane	9	—	[87], this work
— : not reported				

1.4 Motivation and Significance of the research

With the rapid development of technology, higher density and smaller scale electronic devices are urgently needed, leading to continuous reduction in the dimension of functional materials. However, the problem of CMOS compatibility and intrinsic size effect greatly limiting the potential applications of the conventional ferroelectric perovskites in semiconductor and nanoelectronic industries. Also, the transition temperature and the polarization strength of the perovskite-based ferroelectrics gradually decreases with ultrathin film thickness, further hampering their availabilities in modern nanoscale devices. Tremendous efforts were devoted to overcoming the effect of depolarization field in the conventional ferroelectrics and lowering the critical thickness down to less than 10 nm. However, it is still inevitable to select specific electrodes and/or substrates to achieve minimal lattice mismatch. Furthermore, complex fabrication procedures are needed to obtain high-quality thin films with less defects, which largely restricting the promising applications in nanoelectronic and other systems.

Inspired by the extraordinary properties of graphene, a large family of 2D layered materials have subsequently investigated, and significant progresses have achieved in deposition techniques of 2D thin films. Various 2D materials are theoretically predicted the existence of ferroelectricity, but the experimental discovery of ferroelectricity in 2D layered materials is still relatively rare. To date, only around ten different 2D ferroelectric materials have been verified, as summarized in Table 1.1. Still, the origins of the ferroelectric responses are not comprehensively understood. Recently, α-phase In_2Se_3 was demonstrated to exhibit ferroelectricity at room temperature in ultrathin layers. Nevertheless, the performance of ferroelectricity in 2D α-In_2Se_3 at high-temperature environment has not been investigated yet. In this thesis, room-temperature vertical ferroelectricity of multilayer α-In_2Se_3, grown by CVD method, was illustrated and their robust high-temperature ferroelectric phenomena up to 200 °C were sufficiently characterized and examined. Such results reveal the ferroelectric properties in α-In_2Se_3 nanoflakes stably retained at high temperature and represent a new opportunity for 2D materials to apply in high-temperature nanoelectronic devices. Moreover, 2D metal thiophosphate materials are in high research interest as experimental observation of ferroelectricity at room temperature is realized in $CuInP_2S_6$. However, the room-temperature ferroelectricity of $CuInP_2S_6$ and $CuCrP_2S_6$ in 2D limit has not been well explored and awaits further studies. In this work, out-of-plane ferroelectric responses of $CuInP_2S_6$ and $CuCrP_2S_6$ nanoflakes below 10 nm thick were illustrated experimentally at room temperature, promoting the size reduction of future ferroelectric devices and contributing to the family of discovered ultrathin vdW ferroelectric materials.

1.5 Structure of the thesis

The thesis chapters are organized as follows:

Chapter 1: Introduction. This chapter first introduces a general background of typical 2D vdW layered materials with their unprecedented properties and potential applications. Then, the structure of vdW materials and strategies to construct 2D vdW heterostructures are briefly described. Following that, traditional perovskite-ferroelectrics and their recent advances, and other new ultrathin ferroelectric material are illustrated. Lastly, the significance of research is presented to indicate the motivation and objectives of this thesis, and the structure of this thesis is depicted.

Chapter 2: Experimental details. This chapter describes the experimental techniques utilized in the research activities of this thesis. First, the fabrication techniques employed to prepare the ultrathin 2D materials are described. Then, some methods used to assemble vdW heterostructure for characterization are presented. Lastly, various techniques applied to characterize the structures and properties of the fabricated thin films are illustrated.

Chapter 3: Ferroelectricity in two-dimensional In_2Se_3 nanoflakes. This chapter investigates the fabrication of α-In_2Se_3 nanosheets and characterize their structure, out-of-plane ferroelectricity at room temperature and also at high-temperature environments.

Chapter 4: Ferroelectric properties of few-layer ABP_2S_6 nanoflakes. In this chapter, the preparation of two types of ABP_2S_6-structured materials ($CuInP_2S_6$ and $CuCrP_2S_6$) is described. Then, their structure, out-of-plane ferroelectricity at room temperature and physical mechanisms are examined.

Chapter 5: Conclusion and future prospect. The chapter summarizes the results in this thesis. Then, the future prospects of 2D layered ferroelectric materials are proposed.

Chapter 2 Experimental Details

This chapter will present the various experimental techniques employed in this work. Ultrathin α-In_2Se_3, $CuInP_2S_6$ and $CuCrP_2S_6$ nanoflakes were prepared by micromechanical exfoliation and chemical vapor deposition (CVD). The optical characteristics of the samples were examined using optical microscopy and Raman spectroscopy. Their structures and chemical compositions were characterized by second harmonic imaging microcopy (SHIM), X-ray photoelectron spectroscopy (XPS), X-ray diffraction (XRD), transmission electron microscopy (TEM) and energy dispersive X-ray spectroscopy (EDX). The electrical properties were studied through probe station with semiconductor analyzer. The surface topography of the samples was determined using atomic force microscopy (AFM). The nanoscale piezoelectric and ferroelectric responses, and ferroelectric domains were studied and visualized using piezoelectric force microscopy (PFM) at different temperatures.

2.1 Fabrication of 2D ferroelectric nanoflakes

2.1.1 Mechanical exfoliation

Micromechanical exfoliation is a general method to prepare 2D materials with ultrathin thickness (Figure 2.1). In this approach, a sticky tape is used as the media to employ sheer force to the layered bulk crystal and break the weak vdW interactions in between without breaking the strong interlayer covalent bonds. Thinner flakes are peeled off from the bulk crystal onto the tape surface and the exfoliation is repeated several times between two adhesive tape surfaces to achieve atomically thin layers, which are then attached to an arbitrary substrate. As no chemical reaction takes place during the whole procedure, the fabricated ultrathin materials endow with the advantages of clean surfaces and superior crystallinity and are favorable for the study of fundamental physics of the materials.

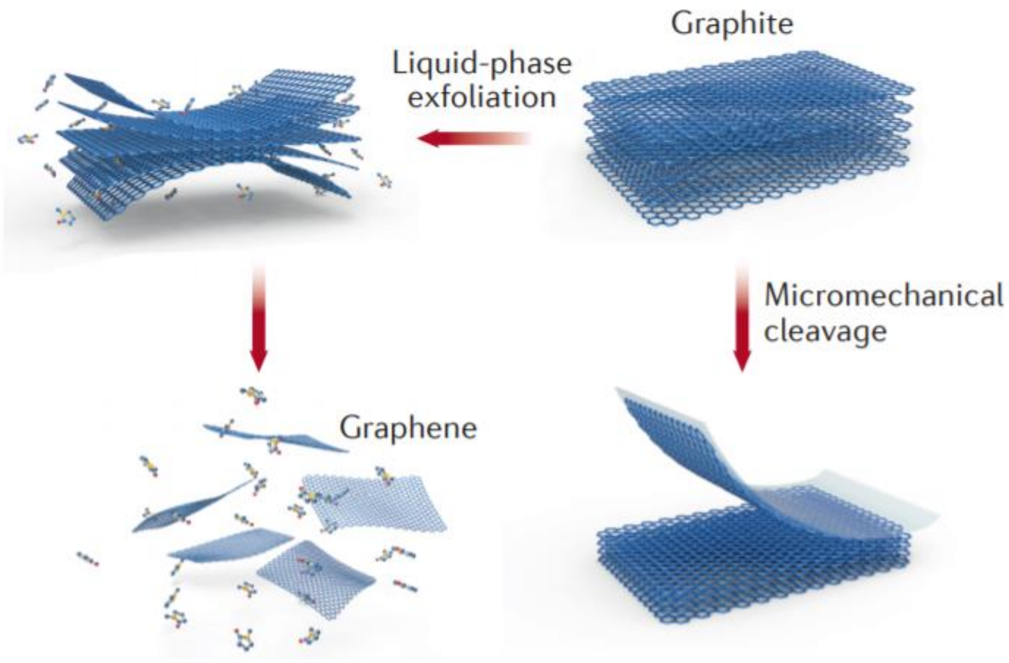

Figure 2.1 Schematic of the preparation of 2D nanoflakes demonstrated by graphite through micromechanical cleavage and liquid-phase exfoliation strategies. [88]

Besides mechanical cleavage via sticky tape, liquid-phase exfoliation is another typical method for fabricating ultrathin 2D materials. This method exfoliates bulk layered materials into 2D nanosheets directly via ultrasonication in a solvent, as shown in Figure 2.1. During this process, the ultrasonic waves allow the delamination of bulk layered crystals by destroying the weak vdW forces between the crystal layers, while the strong covalent bonds are not broken. The yield of the exfoliated 2D nanosheets largely depends on the type of solvents used with various materials. It is experimentally demonstrated that the energy matching of the surface tension between the layered materials and solvents contribute to the reduction of potential energy barrier between adjacent layers and affect the exfoliation efficiency. With a suitable matching, the layered materials can sufficiently adsorb solvent molecules into the interlayer spacings, and the intercalation of solvent molecules will enlarge the spacing between layers, decreasing the interlayer vdW interactions and further delaminating ultrathin 2D nanosheets. In addition, the solvents are essential in the subsequent stabilization of the exfoliated nanoflakes and prevent them from restacking and aggregating. Nevertheless, water, which is a commonly used solvent, is not adequate to exfoliate layered materials efficiently. To enhance efficiency, stabilizers such as polymers and surfactants are added to cooperate with organic solvents in the ultrasonic exfoliation process.

Accordingly, a variety of atomically thin 2D nanosheets including graphene, TMDs and BN are fabricated from their bulk crystal using this approach. The thickness and lateral size of the exfoliated sheets are controllable via adjusting the sonication time, frequency, power and solvents used. After delaminating ultrathin 2D materials, nanosheets with different size and thickness can be selectively achieved by controlled centrifugation. Liquid-phase exfoliation is a relatively low-cost, fast and simple strategy for high-yield and scalable production of 2D nanoflakes and is viable in commercial applications. However, the lateral size of the obtained 2D nanosheets through this strategy is generally small, and the yield of monolayer and few-layer nanoflakes are still not very high. There are also possible residual stabilizers on the exfoliated sheets that are undesirable for further characterizations and applications.

2.1.2 Chemical vapor deposition

Chemical vapor deposition (CVD) is a conventional method that has been extensively used to deposit uniform thin films on substrate surfaces in the modern semiconducting industry. Besides deposition of thin films, CVD is also used to synthesize bulk 3D crystals and materials with zero- and one-dimension with high qualities. In comparison to the mechanical exfoliation method, CVD is a chemical process to fabricate high-quality and uniform 2D nanosheets/ heterostructures on arbitrary substrates with high thickness and lateral size controllability which are feasible for mass production. The operation of CVD is based on the reactions between vaporized precursors and substrate surfaces placed in the CVD system. Generally, one or multiple precursors are heated up to gaseous state in the furnace system and transported to the downstream substrate region by preselected carrier gas, where the precursors are reacted to form the desired product and deposit on the substrate surfaces. There can be one or more heating zones in the CVD system depending on the desired evaporation and deposition conditions of the precursors. The lateral size, thickness and crystal phase of the as-grown films are mainly determined by the type of carrier gas and its flow rate, temperature at different regions, substrate location and growth duration.

Figure 2.2 Homebuilt CVD system consists of two individual furnaces.

In this project, a home-made CVD system consists of two commercial tube furnaces is used for thin film fabrication, and the setup is displayed in Figure 2.2. The use of separate individual furnaces can effectively lower the temperature disturbance between different heating zones of conventional multi-zone furnace systems. The two tube furnaces are monitored and controlled by individual thermocouples and temperature controllers, leading to a precise heating rate of the precursors and good stability of growth temperature. The vapor deposition is carried out in a quartz tube, and the precursors and substrates for synthesis are placed in quartz boats. The upstream of the quartz tube is connected to a digital gas flowmeter to control the flux of the carrier gas into the tube. The pressure of the CVD system is monitored by a gas-pressure meter and vacuum growth condition can be achieved by vacuum pump connected to the downstream of the quartz tube. During thin film deposition, the growth atmosphere can be switched between pure Ar and mix H_2/Ar with the use of a three-way regulating valve. The two heating zones are for different purposes in the deposition of various materials. For example, in the growth of In_2Se_3 ultrathin films, the upstream heating zone is used to evaporate the chalcogenide source (Se) and provide a Se-rich environment in the downstream region. While the downstream heating zone is the main region for the reaction of the chalcogenide and metal precursors to take place and deposition of desired materials on the preselected substrate. Choosing a suitable substrate material is important for the deposition of thin films with desirable crystal structure, thickness and size, and an appropriate gas atmosphere can promote the reaction between precursors

2.1.3 Transfer process

Through the CVD approach, high-quality ultrathin 2D nanosheets can be fabricated in large scale with high controllability. Nevertheless, particular substrates are usually required in match with the deposited materials. For further characterization and device fabrication, transfer of the thin films to other substrates is necessary which often degrades the quality of the deposited nanosheets with additional contaminations and/or wrinkles. Similar to the assembly of vdW heterostructure described in the previous chapter, the CVD-grown nanosheets can be transferred to arbitrary substrates via dry/ wet transfer method with the assistance of different polymers. In this work, the thin films grown by CVD are transferred to various substrates by polystyrene (PS)-assisted wet transfer strategy.

2.2 Characterization of ultrathin ferroelectric materials

2.2.1 Optical microscopy

Optical microscopy is a simple and fast technique to primarily observe the surface topography and thickness and phase of 2D materials. The optical microscope system generally utilizes a set of lenses to focus light on the sample surface and generates images of different magnifications by collecting the reflected light from the surface.

Under the optical microscope, when light is illuminated on different materials, it interferes differently and produces optical contrast, images are then formed by collecting the reflected light and 2D materials and substrates can be distinguishable. Besides, the optical transparency of 2D materials varies with their thickness and the thickness contrast of 2D nanoflakes can be obtained using optical microscopy. For 2D materials with a high variation of optical path and optical transparency, the color and reflected light intensity can be used quantitively to determine the thickness of the nanoflakes.

Second-harmonic imaging microscopy (SHIM) is a simple, rapid and non-contact optical technique based on a nonlinear optical phenomenon known as second-harmonic generation (SHG) which can only be induced by materials with an inverse symmetry breaking structure. When photons are emitted on a non-centrosymmetric material, two photons with the same frequency ω interact with the material and then "combined", forming a new emitted photon with twice the frequency (2ω) of the incident photons (and the wavelength is halved). In SHIM, a high-intensity light source with a frequency of 2ω is used to excite coherent SHG signals and emitted photons near the frequency ω are collected to construct second-harmonic images. In this work, the symmetry of 2D layered ferroelectric materials is inspected under Leica TCS SP8 MP confocal microscopy.

2.2.2 Raman Spectroscopy

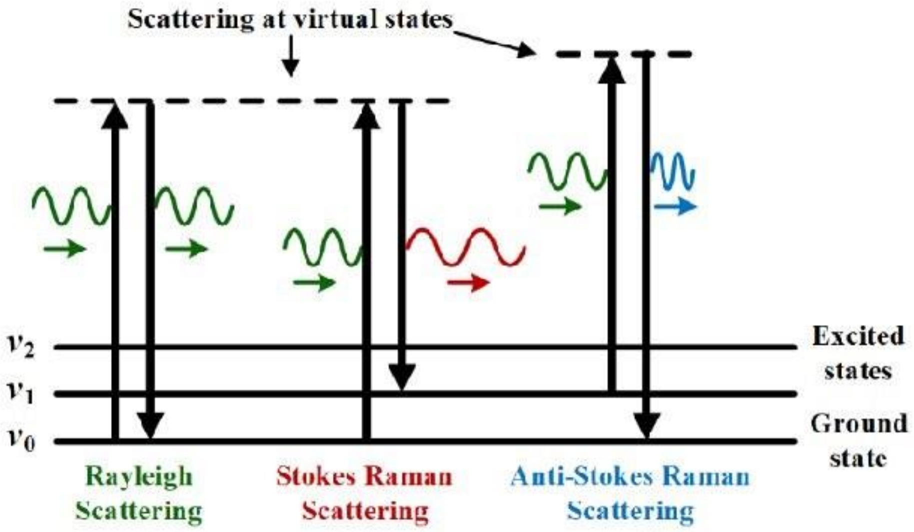

Figure 2.3 Basic working principle of Raman spectroscopy. [89]

Raman spectroscopy is another non-destructive technique to employ light for characterizing the structure, phase and crystallinity of materials. The working principle of Raman spectroscopy bases on the scattering of the emitted laser light and molecules in the material under observation as described in Figure 2.3, and the vibration modes of the material are collected for analysis. During measurement, a laser light source is emitted onto the sample and interacts with the molecules. The molecules from high intensity resting in the ground state (lowest energy state) are excited by the incident laser photons to a virtual state with higher energy. The molecules are then returned to a lower energy state with the emission of photons. If the molecules return to the original ground state, the emitted photons are identical to the incident photons and this process is called Rayleigh elastic scattering. As the incident and emitted photons are identical, Rayleigh scattering gives no useful information about the structure of the materials. If the molecules return to a lower energy state differing from the original state, the emitted photons will have energy different from the incident photons, which is called Stokes Raman scattering and anti-Stokes Raman scattering (inelastic scattering). Since the emitted photons have a different energy than the incident photons, there will be a wavelength shifting in the inelastically scattered photons. Anti-Stokes Raman scattering can only happen in molecules initially at an excited state, and the possibility for the occurrence of Stokes Raman scattering is much higher than that for anti-Stokes Raman scattering. Hence, the Raman spectrum is constructed mainly on the basis of high-intensity Stokes Raman scattering. The Raman spectroscopy provides a unique fingerprint to identify different materials, with information about the chemical structure and phase.

The Raman spectra analyzed in this work are conducted by Witec Alpha 300 R confocal Raman system equipped with 532 nm excitation laser source, which penetration depth is about a few hundred nanometers. Besides single-point measurement, this confocal Raman system is also available for large-area Raman mapping on the selected position of the sample.

2.2.3 X-ray Photoelectron Spectroscopy

Photoelectron spectroscopy is an experimental technique for measuring the energy of photoelectrons emitted from the surface of the sample on the basis of photoelectric effect to examine the chemical composition of materials and/or to characterize the bonding in molecules. The excitation sources include X-ray and ultraviolet (UV) light for different measuring purposes. In different types of photoelectron spectroscopy, a high vacuum is required for measurements to avoid scattering between air and the photoelectrons.

X-ray photoelectron spectroscopy (XPS) is a quantitative technique to measure the elemental composition of a material and determine the ratio and oxidation state of elements existing in the material. XPS has a penetration depth of about 10 nm and is sensitive to the elements near the surface of the material. When the X-ray source is illuminated on the sample surface, the photons are absorbed by the electrons inside the atoms exist within the sample. As the X-ray photons have high energy, the excited electrons can escape away from the atoms and become photoelectrons with certain kinetic energy. In the XPS system, a monochromatic X-ray excitation source with fixed photon energy is used. Therefore, the kinetic energy of the emitted photoelectrons relates only to the work function of the atoms and the atomic orbital of the electrons.

For every element, the set of photoelectron energy is characteristic which corresponds to the electronic configuration. Through analyzing the energy and number of photoelectrons emitted from the sample, the elemental composition and ratio can be directly identified. The XPS measurements in this work are conducted using the Nexsa XPS system.

2.2.4 X-ray diffraction

XRD is an important technique for rapidly determining the structure of crystalline materials in a non-destructive way. The working principle of XRD is illustrated schematically in Figure 2.4, which is based on constructive interference of the monochromatic X-rays incident on the crystalline sample surface. The interaction of incident monochromatic X-rays on the analyzed samples generates constructive interference (be diffracted) only when the condition of Bragg's Law is satisfied: $2d_{hkl}\sin\theta = n\lambda$, where θ is the diffraction angle, λ is the wavelength of incident X-rays, h, k, l are the Miller indices, and d_{hkl} is the distance between adjacent lattice planes (h k l) of the samples. The diffracted X-rays are then collected and counted, a diffraction pattern can be built bases on the diffraction angles and number of counts. The diffraction spectra can offer various structural information about the measured samples such as crystal structure, phase, orientation and lattice spacings. The XRD patterns of crystalline materials analyzed in this thesis are conducted using a Rigaku Smartlab 9 kW X-ray diffractometer equipped with a 2D detector, and X-ray source from Cu *Kα* radiation (λ = 0.154 nm).

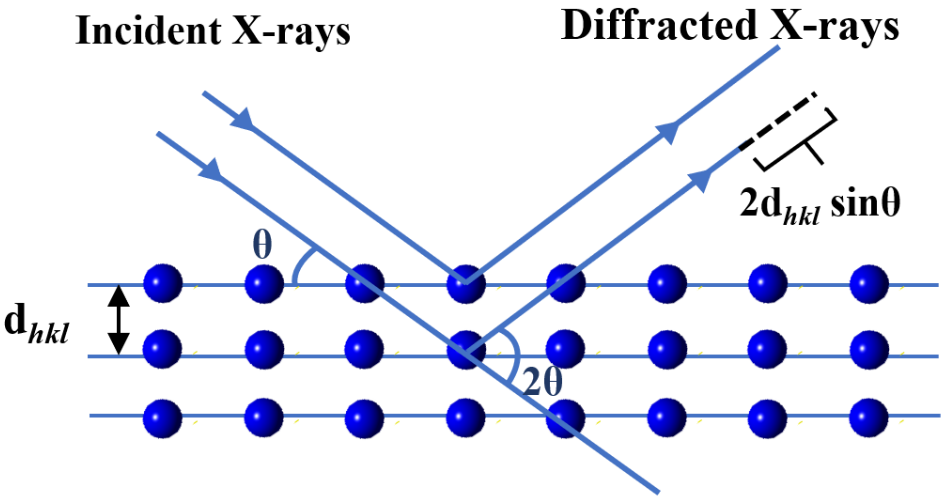

Figure 2.4 Schematic of operating principle of XRD.

2.2.5 Transmission electron microscopy

Transmission electron microscopy (TEM) is a powerful and important technique for the characterization of 2D materials at the atomic scale. Instead of light, TEM uses high energy electron to form images with significantly higher resolution than optical microscope as the de Broglie wavelength of electron is much shorter than the wavelength of light. In TEM, a focused electron beam is irradiated on the sample specimen and the electrons transmitted through the specimen are used to create an image. To allow the transmission of electrons, the sample is always thinned down to less than 100 nm thick. TEM can be operated in two basic modes which are the imaging and diffraction modes. For real-space imaging, there exist several contrast mechanisms to create an image including mass-thickness contrast, diffraction contrast and phase contrast imaging. These contrast mechanisms are able to provide different types of information about the sample, such as chemical composition, the difference in thickness, crystallinity, crystal orientation, lattice structure, etc. By adjusting the lenses so that the back focal plane of the lens is placed on the imaging apparatus, the operation mode can be switched to diffraction mode and diffraction pattern can be observed on the viewing screen. The generated diffraction patterns of crystalline, polycrystalline and amorphous materials are dissimilar and the crystallinity of the area under illumination can be determined. For single-crystalline materials, the diffraction pattern depends on the structure and orientation of the selected area and offers information about space group symmetry of the lattice.

The high-resolution TEM images and selected area electron diffraction (SAED) patterns of the 2D materials discussed in this thesis are achieved using JEOL 2100F TEM device as shown in Figure 2.4, which is consisted of electron gun chamber, sample chamber, and projection chamber and are maintained at ultrahigh vacuum environment. During characterization, the electron beam is accelerated by a voltage of 200 kV and an exposure time of 0.5 s.

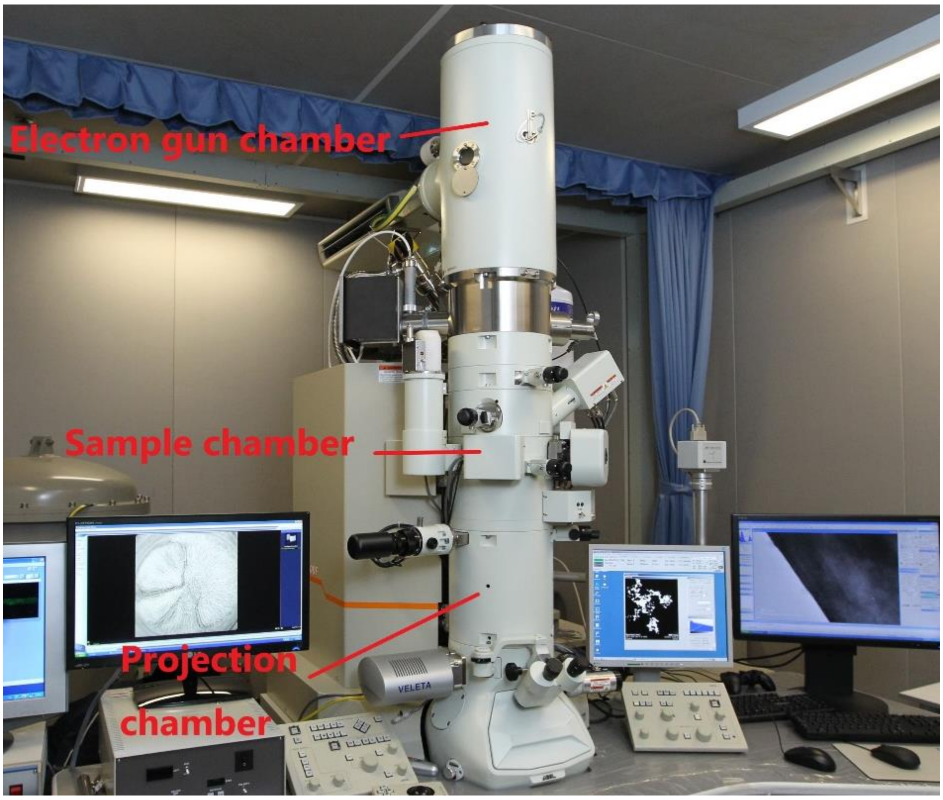

Figure 2.5 Image of the TEM system used in this work.

2.2.6 Energy dispersive X-ray spectroscopy

Energy dispersive X-ray spectroscopy (EDX) is a technique used for chemical microanalysis of materials and are generally in-built in electron microscopy. By mounting energy dispersive X-Ray detector in the electron microscope, characteristic X-rays emitted from the sample during bombardment of electron beam, as described schematically in Figure 2.5, can be measured and elemental composition of the target sample can be characterized. When the electron beam bombards on the sample, inner shell electrons are kicked out as secondary electrons, and the holes are filled by electrons from the outer shell with higher energy. The shift of electrons from high to low energy level generates high energy X-ray photons and are collected by the X-ray detector. Each element possesses a characteristic electronic structure and has a unique set of characteristic X-ray peaks. Therefore, EDX can be used to directly distinguish the elemental composition of samples.

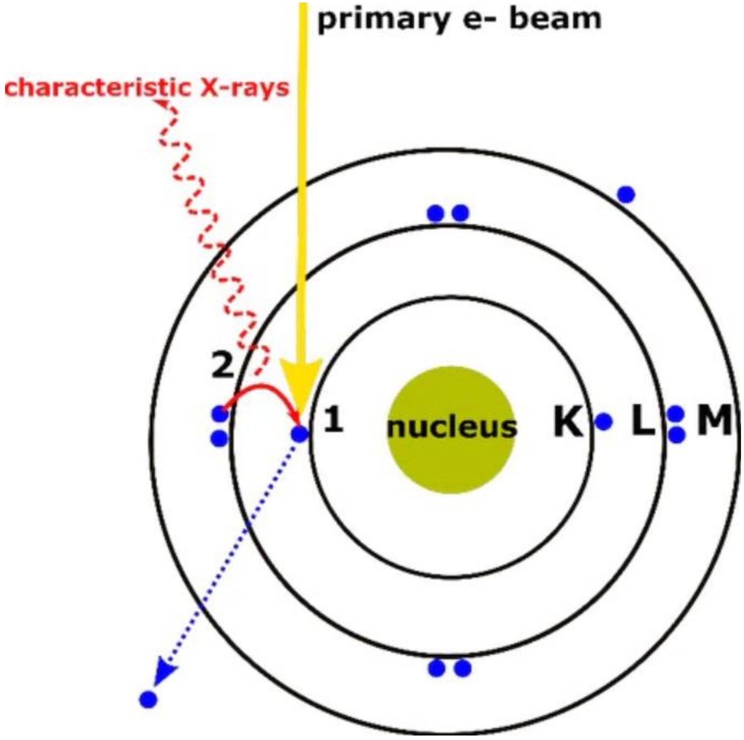

Figure 2.6 Schematic diagram of the generation of characteristic X-rays for EDX. [90]

2.2.7 Probe station with semiconductor analyzer

The probe station system is mainly composed of optical microscope, probe station, and semiconductor parameter analyzer and is a typical technique for measuring the electrical characteristics of fabricated semiconducting devices. For measurements, the devices are positioned on the probe station and tungsten probes are employed to contact the electrodes of the devices and connect the devices to the analyzer. The optical microscope mounted within the probe station can help to identify and locate the electrodes of the devices. In this work, Keithley 4200-SCS semiconductor parameter analyzer is used to offer a voltage source and acquire the current responses of the devices with an ultrahigh current resolution at femto ampere scale.

Figure 2.7 Image of the probe station used in this work.

2.2.8 Scanning probe microscopy

Scanning probe microscopy is a group of powerful tools used to study a variety of properties and characteristics of materials at the atomic scale including atomic force microscopy (AFM), piezoelectric force microscopy (PFM), kelvin probe force microscopy (KPFM), magnetic force microscopy (MFM) and so on. The operation of SPM is based on the measurement of the different types of interaction forces between a physical probe and the surface of the scanned sample.

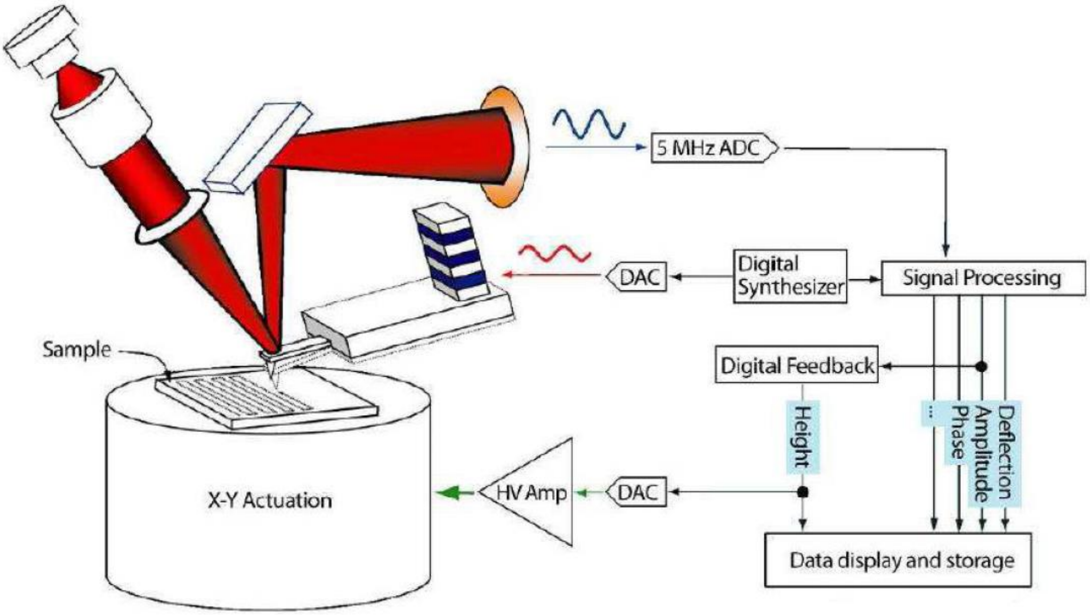

Figure 2.7 Schematic of tapping mode imaging.

Among the SPM family, AFM is the most used model for measuring the topography, height, surface roughness and phase contrast of the surface of materials. Typically, a physical probe with very a sharp tip is used to scan back and forth over the sample surface at a very short distance to form an image. The probe is attached to a cantilever that will deflect when the tip approaches the surface due to the interaction force in between. The deflection of the cantilever is measured by a laser beam focusing on it and the reflected beam is detected by a photodiode to track the change in position of the laser beam. AFM can operate in three different modes which are contact mode, tapping mode and non-contact mode. Contact mode measures the repulsive force between tip and sample surface at a very close distance and delivers the highest accuracy as repulsive force is very sensitive to distance. But keeping the tip very close to the surface can easily damage the sample and distort the measured data. Non-contact mode measures the attractive force and the tip is maintained at a certain distance away from the sample surface, but the image resolution is the lowest among the three operating modes. In this work, tapping mode is employed which can achieve high-resolution images without causing damage to the sample. The working principle of tapping mode in AFM is described in Figure 2.6. The tip is oscillating near its resonance frequency by a small piezoelectric actuator in the cantilever. The oscillatory motion of the cantilever is detected by the photodiode and the electronic components inside the controller measure the amplitude and phase of the oscillating signal with respect to the driving signal.

PFM is an effective and direct technique to observe ferroelectric domains in ferroelectric materials and demonstrate the existence of ferroelectricity in ultrathin 2D ferroelectric materials. In general, a sharp conductive probe is used to scan over the sample surface in contact mode. An AC bias is applied to the tip to cause a strain to the surface which in turn leads to periodic deflection of the cantilever through the inverse piezoelectric effect. The inverse piezoelectric effect usually induces a change in the amplitude of the signal, but the piezo signals can be very small, with just a few picometers per volt of applied bias. Therefore, frequency close to the contact resonance of the conductive probe is selected to amplify the small piezo signals. For ferroelectric materials, the local polarization will cause a phase change of the signal which depends on the orientation of the polarization, and ferroelectric domains can be observable in the phase image. The PFM measurements in this work are conducted by Asylum MFP-3D Infinity device in dual AC Resonance-tracking (DART) mode (Figure 2.7). By tracking two frequencies on each side of the contact resonance frequency peak, the driving frequency can better be maintained near contact resonance and response signals can be significantly enhanced. By using lock-in amplifiers, the phase and amplitude of the signal can be measured simultaneously, and the topography and ferroelectric domains of the sample can be imaged at a time.

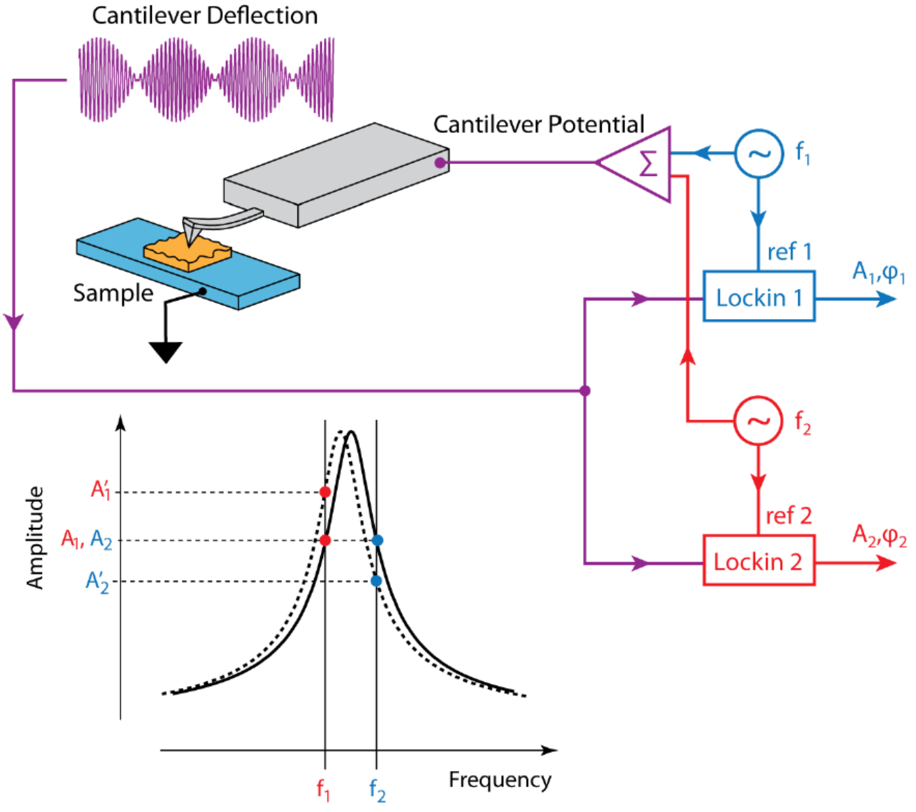

Figure 2.8 Setup of the DART mode in PFM.

Chapter 3 Ferroelectricity in Two-dimensional In_2Se_3 Nanoflakes

3.1 Introduction

In the past decades, conventional ferroelectric perovskite oxides have been extensively demonstrated their feasibility to apply in various devices [49, 52, 54]. The pursuance for high-density and high-capacity devices and the rapid technology progresses have intensively promoted the research on the size reduction of the ferroelectrics. However, the ferroelectricity of the traditional perovskite ferroelectrics will disappear at a critical thickness due to the intrinsic size effect [55, 57]. Moreover, the Curie temperature T_c and polarization strength significantly deteriorate when their thickness approaches to 2D limit, which largely restricting their potentials in high-density and high-temperature device applications [91, 92]. In recent years, great efforts are drawn to address the fundamental depolarization effect in traditional ferroelectrics [55, 56, 59]. By theoretical calculations, it is shown possible to preserve ferroelectricity in traditional ferroelectrics above room temperature with thickness down to a few nanometers. Nevertheless, matching of specific electrodes and/or careful selection of substrates with small lattice mismatch to that of the ferroelectric materials are necessary to retain atomic-scale ferroelectricity. The constraints of lattice mismatch and incompatibilities between materials lead to limited possibilities to apply in nanoelectronics [62].

Recently, a large amount of research works is conducted to investigate new ferroelectric materials besides conventional perovskite ferroelectric oxides, including Hf/ZrO_2-based system and various types of 2D materials. In the past ten years, 2D vdW layered materials have developed rapidly and possess different excellent properties, which offer numerous opportunities to overcome the finite size effect issue of typical ferroelectric materials and realize ferroelectricity in monolayer limit. To date, plenty of 2D layered ferroelectric materials have been predicted with theoretical calculations, for example single-layer group IV chalcogenides (SnS, SnSe, etc.) [71], elemental group V monolayers [72], distorted monolayer 1*T*-phase TMDs [11, 73], transition metal thiophosphate ($AgBiP_2Se_6$, $CuInP_2S_6$, etc.) [74], III_2–V_3 compounds (In_2Se_3, etc.) [76] and so on [93, 94]. In contrast, experimental discovery of ultrathin layered ferroelectric materials still remains scarce, which just around ten 2D ferroelectric materials are currently reported including SnTe, β′-In_2Se_3, SnS, BA_2PbCl_4, $CuInP_2S_6$, distorted 1*T*-$MoTe_2$, WTe_2 and α-In_2Se_3 [77-83, 85, 95].

In particular, most of the experimentally confirmed 2D layered materials are either with in-plane (IP) or out-of-plane (OOP) ferroelectricity, while α-In_2Se_3 is currently the only reported 2D ferroelectric material that exhibits ferroelectricity in both directions down to single-layer thick [85, 95-99]. Besides, the Curie temperature of $CuInP_2S_6$ is just at ~42 °C, and that of WTe_2 and $MoTe_2$ is above room-temperature (around tens of degree Celsius) [82, 83, 100]. In comparison, the transition temperature of few-layer α-In_2Se_3 can reach above 400 °C demonstrated with temperature-dependent SHG spectra, much superior to the other 2D vdW ferroelectric materials [84].

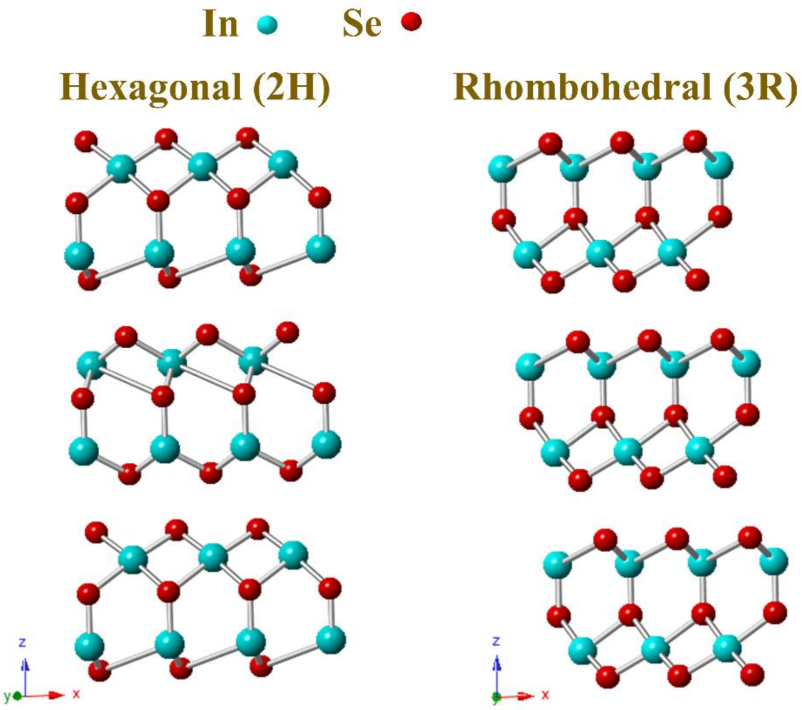

Figure 3.1 Crystal structure of 2H and 3R α-In_2Se_3.

In_2Se_3 exists in nature five phases (α ,β, γ, κ , δ) with different crystal structure at various temperatures [101]. Among five, both α-phase, β-phase and κ-phase have a layered vdW structures. The bulk In_2Se_3 owns a moderate direct bandgap at around 1.3 eV and shows high potential in optoelectronic applications. Yu's group [102] illustrates the outstanding photoresponse of multilayer α-In_2Se_3-based photodetector which gives an external quantum efficiency of 163000 % at 5 V and photoresponsivity of 395 A W^{-1} with 300 nm wavelength of light source, much higher than the performance of graphene and other semiconductors (MoS_2 & GaSe)-based photodetectors. Furthermore, the bandgap of α-In_2Se_3 increases when the thickness approaches 2D limit, which rises from ~1.3 to 1.55 eV from bulk crystal to monolayer α-In_2Se_3 at room temperature.

As described in the previous chapter, spontaneous polarization in ultrathin ferroelectric materials is associated with a non-centrosymmetric crystal structure that forms electric dipoles in the materials. Although several stable polymorphs of In_2Se_3 are layered materials, only α-In_2Se_3 exists a stable non-centrosymmetric structure at room temperature and contributes to 2D ferroelectricity in IP and OOP directions. The spontaneous polarization initiates from the off-centering Se atom in the middle of the quintuple (Se−In−Se−In−Se) layers. Particularly, α-In_2Se_3 exhibits two distinct stacking arrangements: hexagonal (2H) and rhombohedral (3R) structures, as depicted in Figure 3.1. Both stackings are experimentally shown with the existence of intercorrelated IP and OOP ferroelectricity at room temperature [78, 85, 95-99]. Different kinds of electronic devices are thereby fabricated on 2D α-In_2Se_3 basis such as ferroresistive Schottky diodes and ferroelectric field-effect transistors, allowing a broad diversity of applications as nanoscale optoelectronics and non-volatile memory devices. Although α-In_2Se_3 owns various outstanding properties, its ferroelectric properties at high-temperature range are not yet explored which are essential for high-temperature device applications. In this chapter, the fabrication process of 2D α-In_2Se_3 thin films via CVD method is illustrated. We observe the intrinsic OOP ferroelectricity in deposited α-In_2Se_3 nanosheets under PFM in a wide temperature range up to 200 °C. We also study the thickness-dependence of the coercive field of α-In_2Se_3 and examine the coercive field behaviors at different temperatures.

3.2 Chemical vapor deposition of ultrathin In_2Se_3 nanosheets

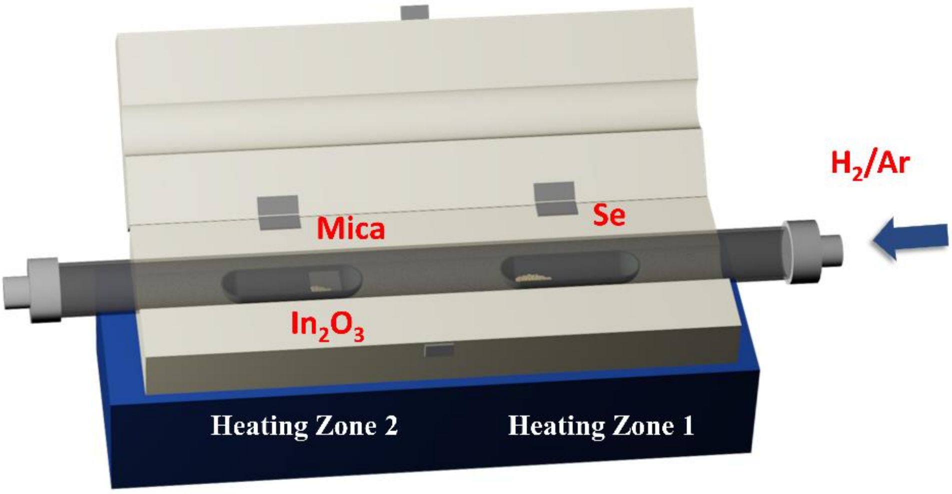

Figure 3.2 Schematic of CVD system for the growth of α-In_2Se_3 nanosheets.

Several deposition techniques such as CVD and MBE are developed to grow large-scale α-In_2Se_3 thin films. In the present work, CVD approach is used to synthesize α-In_2Se_3 nanosheets and the schematic diagram of the CVD system is as shown in Figure

3.2. Different growth conditions (growth temperature and duration, location of substrate, amount of precursors etc.) were attempted and optimized to fabricate uniform and high-quality nanosheets. The finalized growth parameters are summarized in Table 3.1 and one possible combination of growth temperature and time is as shown in Figure 3.3. As shown in Figure 3.2, a high purity selenium source on quartz boat is placed at the center of heating zone 1 to heat up to 270-300 °C. In_2O_3 powder is put onto another quartz boat and heated up to 660-700 °C and the growth temperature is held for 15 to 40 min in atmospheric pressure. 10% H_2/Ar mix gas is used as the carrier gas and the flow rate is maintained throughout the deposition process as hydrogen can encourage the reaction between Se and In_2O_3 precursors to form In_2Se_3. The carrier gas flows into the quartz tube only after the temperature of the two heating zones arriving proper growth temperature in order to maintain a high-concentration selenium source at the reaction site, and H_2/Ar mix gas is flowing at a flux of 8-10 sccm. Mica substrate is selected as the deposition site instead of other typical substrates, such as SiO_2, as it possesses a dangling bond-free surface which promotes lateral deposition of In_2Se_3 to form thin films. The substrate is placed above the In_2O_3 powder to deposit In_2Se_3 nanosheets and the CVD furnace is cooled down naturally to room temperature after growth.

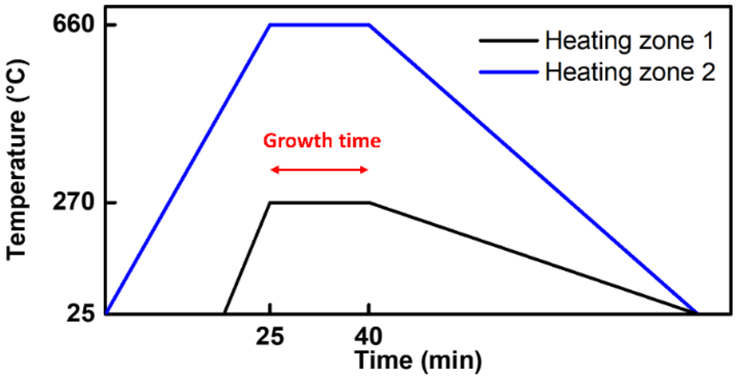

Figure 3.3 Temperature versus time profile of CVD synthesis of α-In_2Se_3.

Table 3.1 Summary of deposition conditions of 2D α-In_2Se_3

Growth temperature of heating zone 1	270-300 °C
Growth temperature of heating zone 2	660-700 °C
Growth duration	15-40 min
Carrier gas flow rate	8-10 sccm
Amount of In_2O_3 precursor used	1-3 mg
Amount of Se precursor used	50-100 mg

The as-grown samples were first observed under optical microscopy for their shape and surface morphology. Figure 3.4 displays the optical images of In_2Se_3 samples deposited on mica substrates at the same evaporation temperature (270 °C and 660 °C respectively) and amount of the precursors but different carrier gas flux and growth time interval. The color contrast in these images represents a thickness variation of the fabricated nanosheets. The samples as shown in Figure 3.4 (a) were deposited with mix gas flowing at 30 sccm and kept at growth temperature for 30 min. The obtained samples are relatively small in lateral dimension, most of which are just a few micrometers. The gas flow rate for growing the samples as shown in Figure 3.4 (b) was reduced to 10 sccm to increase the concentration of chalcogenide precursor in heating zone 2 and the growth duration was increased to 40 min. In_2Se_3 films with a much larger size were deposited. These films start to merge together to be a continuous film and multiple layers of In_2Se_3 with different crystal orientations are formed. This is probably due to too long growth period so that extra layers are deposited on top of the In_2Se_3 films. With a shorter growth duration of 25 min, the quality of the deposited nanosheets are efficiently enhanced. The proportion of multilayer In_2Se_3 are effectively lowered and more single-crystalline In_2Se_3 triangles can be observed with lateral dimension of ~10 μm (Figure 3.4(c)). Besides, it is observable that small granules were formed at the center and edges of the nanosheets which possibly deposited during the cooling down of CVD system. This phenomenon can be improved by turning the atmosphere into pure argon right after the deposition process. At a further reduced carrier gas flux and growth duration (8 sccm for 15 min), ultrathin In_2Se_3 triangles with a largest lateral dimension of 50-100 μm were fabricated without the formation of small granules (Figure 3.4(d)). The results suggest that the concentration of selenium source at the reaction region and growth duration are critical factors for achieving high-quality and large-size In_2Se_3 nanosheets.

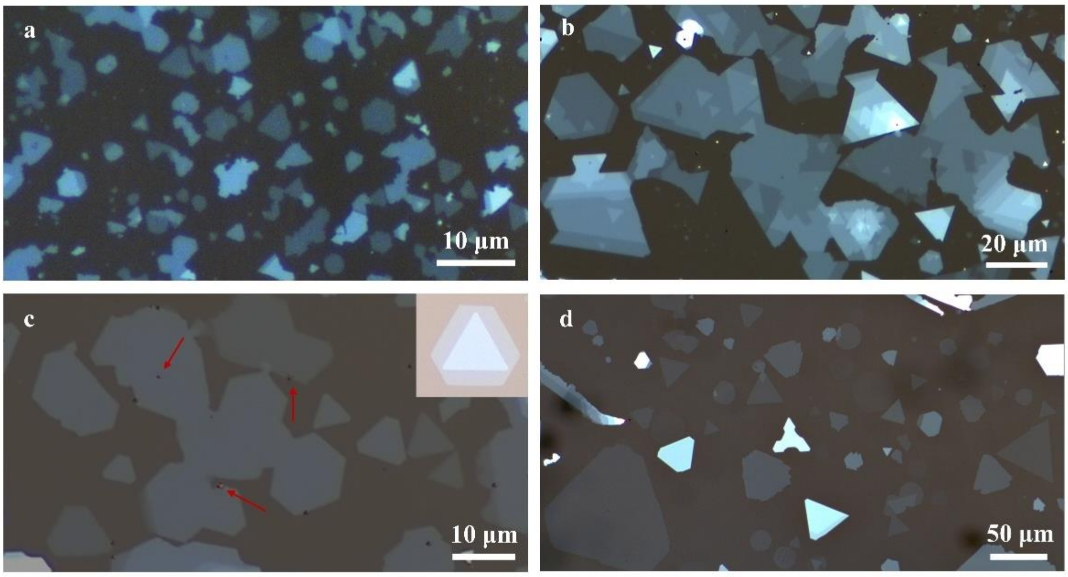

Figure 3.4 Optical images of deposited In_2Se_3 films under different growth conditions. (a) Gas flowing at 30 sccm for 30 min, (b)10 sccm for 40 min, (c) 10 sccm for 25 min and (d) 8 sccm for 15 min.

Besides varying the growth duration and rate of gas flow, deposition of In_2Se_3 films under different evaporation temperatures and amount of precursors were also attempted for optimization of growth parameters. At a temperature range of 640 -720 °C, the deposited samples showed no obvious difference in thickness or morphology. The selenium precursor was always kept in an excess amount of ~50-100 mg relative to that of In_2O_3 precursor. It was also noticed that amount of In_2O_3 powder affects the growth time for high-quality thin films, in which a longer time is required for selenization of metal precursor before deposition to happen if a larger amount of metal precursor is used in each synthesis. Therefore, the amount of In_2O_3 powder used in each fabrication was controlled at a small amount of ~1-3 mg. Through numerous attempts, the optimal growth parameters for In_2Se_3 nanosheets in this work are summarized in Table 3.1.

The topography of CVD-grown In_2Se_3 thin films was further determined using AFM with accurate thickness information measured. As previously reported, single-layer In_2Se_3 has a thickness of about 1 nm [76]. Figure 3.5 demonstrates the AFM topographic images of ultrathin In_2Se_3 films and the corresponding height profiles. Deposited undesirable granules on an In_2Se_3 film of 4.7 nm thick (corresponds to five In_2Se_3 layers) are clearly visible in Figure 3.5 (a). Under optimized growth conditions, high-quality In_2Se_3 triangles can be deposited on mica substrates. Figure 3.5 (b) and (c) show the surface morphology of tri-layer and monolayer In_2Se_3 nanoflakes with a smooth surface and sharp edges without the formation of granules, indicating they are single-crystallized in good quality.

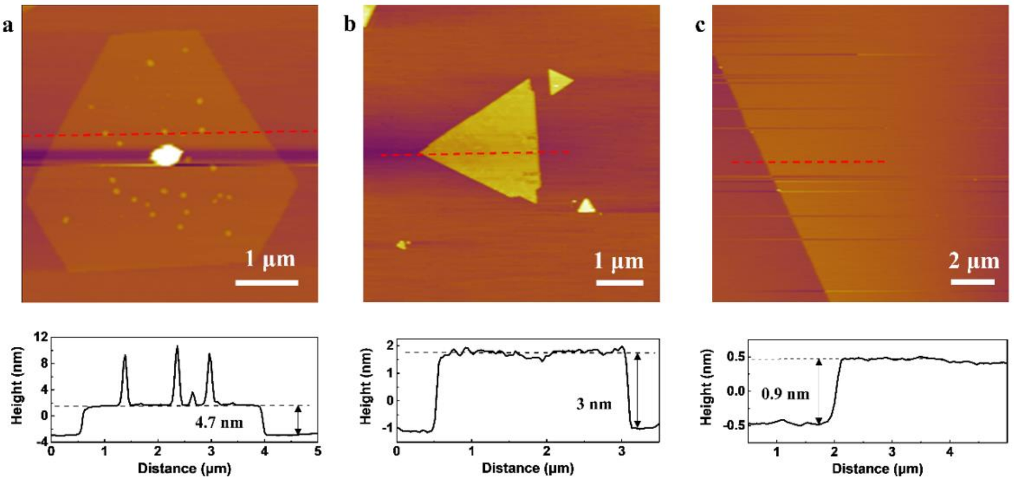

Figure 3.5 (a-c) AFM images and corresponding height profiles of different ultrathin In_2Se_3 films grown at various conditions.

3.3 Structural characterization of In_2Se_3

The crystal structure and phase of the In_2Se_3 thin films were identified via a confocal Raman spectroscopy using an excitation laser with 532 nm wavelength and 1 μm spot size. As illustrated in Figure 3.6 (a), three dominant peaks are recognized from the Raman spectrum of as-grown In_2Se_3 samples at ~107, 170 and 203 cm^{-1}, attributed to the A_1 (LO+TO), A_1 (TO) and A_1 (LO) vibrational modes of α-phase In_2Se_3, respectively. The measured results are consistent with the previously reported values [95, 97]. Moreover, the Raman peak at ~90 cm^{-1} always occurs in 2H α-In_2Se_3, and usually vanishes in 3R α-In_2Se_3 and therefore can be used for determining the structure of the α-In_2Se_3. The disappearance of Raman peak at ~90 cm^{-1} verifies that the CVD-grown In_2Se_3 nanosheets in this work were in 3R structure. Besides, Raman mapping of the α-In_2Se_3 triangle (Figure 3.6 (b)) was obtained by plotting the Raman intensity at 107 cm^{-1} under 532 nm excitation laser of 0.3 mW power, further confirming the uniformity and pure α-phase of CVD-grown In_2Se_3 nanosheets in this work. The symmetry of α-In_2Se_3 samples was determined using SHIM. Figure 3.6 (c) presents the SHG image and corresponding SHG signal of multilayer α-In_2Se_3 triangles at room temperature using an excitation laser source of 900 nm wavelength, confirming the non-centrosymmetric crystal structure of the fabricated In_2Se_3 nanosheets which is the origin of ferroelectricity in α-In_2Se_3.

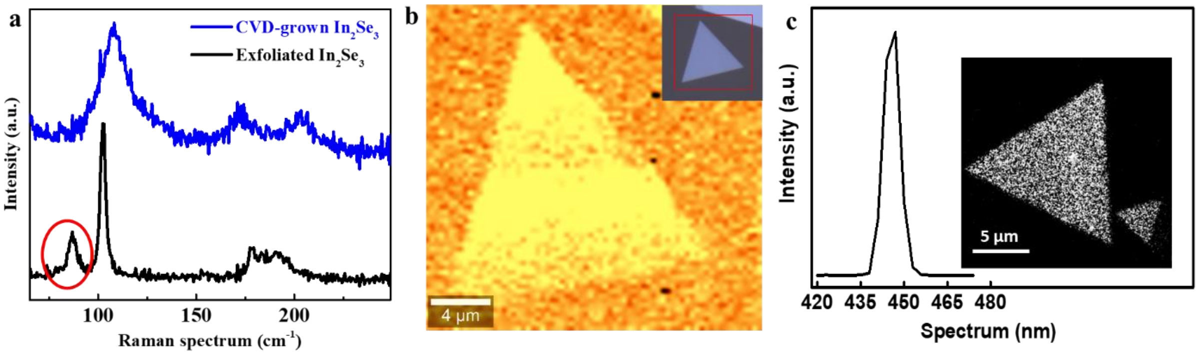

Figure 3.6 (a) Raman spectra of CVD-grown In_2Se_3 nanosheets on mica substrate and exfoliated In_2Se_3 samples on SiO_2 substrate. (b) Raman mapping of the as-grown In_2Se_3 triangle with excitation laser wavelength of 532 nm, inset: optical image of the Raman mapped area. (c) SHG image and corresponding SHG spectrum of few-layer α-In_2Se_3 triangles.

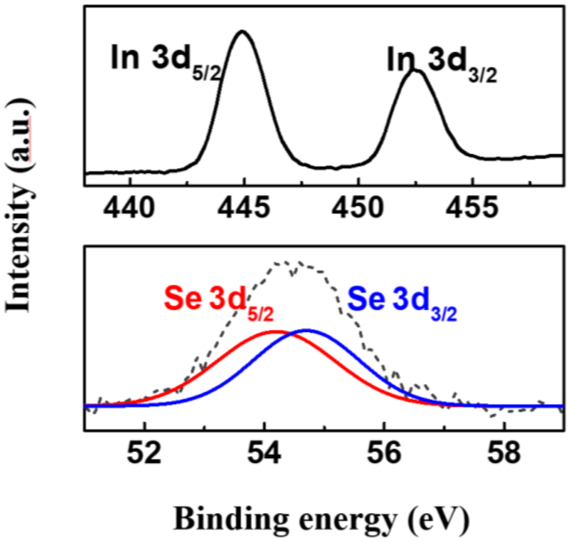

Figure 3.7 XPS spectra of In-3d (up) and Se 3d (down) core levels of 2D In_2Se_3 thin films.

XPS measurement was carried out to investigate the elemental composition of the as-grown α-In_2Se_3 thin films and the results are presented in Figure 3.7. Strong XPS doublets at 444.9 and 452.6 eV correspond to the In $3d_{5/2}$ and In $3d_{3/2}$ core level orbitals, respectively, and the pair of peaks at 54.2 and 54.7 eV are attributed to the Se $3d_{5/2}$ and Se $3p_{3/2}$ orbitals respectively, indicating the chemical composition of the as-grown nanosheets.

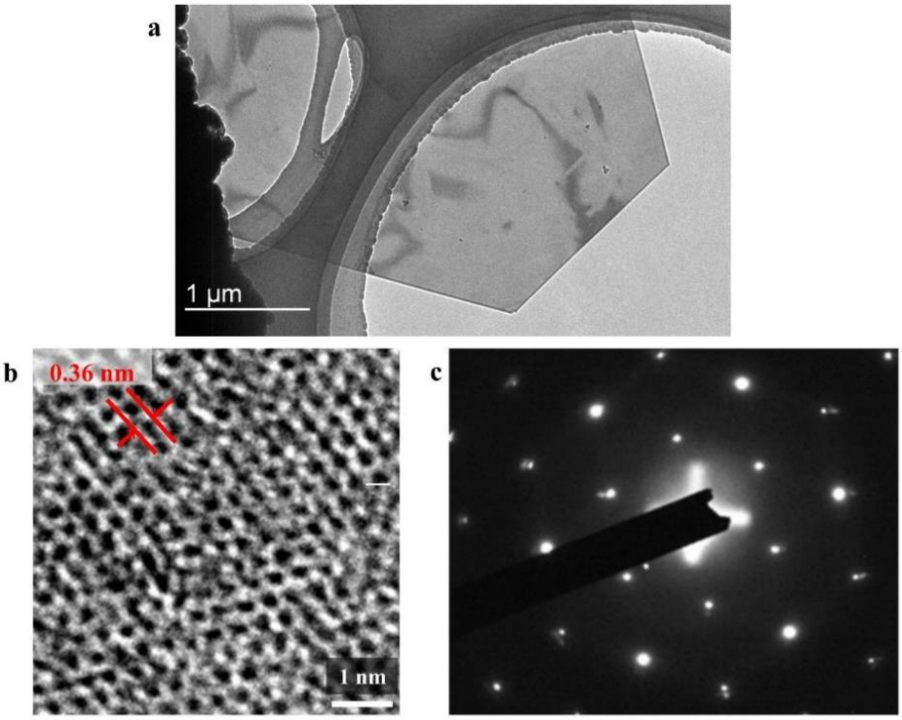

Figure 3.8 (a) Low-resolution and (b) high-resolution TEM images of ultrathin α-In_2Se_3 film, and (c) corresponding SAED pattern.

The crystallinity and atomic structure of In_2Se_3 nanosheets were analyzed via TEM. The specimen was prepared using PS-assisted wet transfer technique to transfer In_2Se_3

nanosheets from the mica substrate to the TEM copper grid. In this method, a layer of PS solution was spin-coated onto the sample surface at 2500-3000 rpm for 30 s and baked at 150 °C for 5 min. With the assistance of water, the PS/ In_2Se_3 film was peeled off from mica substrate and placed onto TEM grid. After the transfer process, PS layer was dissolved in toluene, leaving only In_2Se_3 nanoflakes on the target grid. Figure 3.8(a) demonstrates a low-resolution TEM image of In_2Se_3 film transferred on the copper grid for TEM measurement. Figure 3.8(b) displays a high-resolution TEM (HRTEM) image of the top-view of α-In_2Se_3 with a uniform and periodic hexagonal crystal lattice and a lattice spacing of ~0.36 nm. Also, the corresponding selected area electron diffraction (SAED) pattern (Figure 3.8(c)) presents a 6-fold symmetry, both indicating a high crystallinity of fabricated samples.

3.4 Ferroelectric characterization of In_2Se_3

PFM is an effective system for illustrating the presence of spontaneous polarization and ferroelectric domain in nanoscale samples. Therefore, it was performed to investigate the ferroelectric properties of the ultrathin α-In_2Se_3 in this work. In all PFM measurements, ferroelectric phenomena of α-In_2Se_3 were demonstrated through α-In_2Se_3/Pt structures that constructed by transferring ultrathin α-In_2Se_3 samples onto conductive Pt substrates by similar PS-assisted wet transfer strategy for preparation of TEM specimens.

3.4.1 Room-temperature ferroelectricity

PFM phase and amplitude responses can be used to manifest the direction of polarization and local piezoelectric responses of measured ferroelectric materials. Figure 3.9(a) shows the topography image of an 8 nm thick α-In_2Se_3 nanosheet that cracked during the wet transfer process from mica to Pt substrate, and the height profile is illustrated in Figure 3.9(c). A phase contrast difference in the OOP direction was clearly distinguishable (Figure 3.9(b)), demonstrating a single ferroelectric domain in the α-In_2Se_3 triangle. Reversal of the polarization direction by external electric field is one of the main features for ferroelectric materials. Figure 3.10 (a) displays the OOP PFM phase and amplitude hysteresis loops of the 8 nm α-In_2Se_3 scanned by dc triangular waveform from -8 V to 8 V. The off-field phase hysteresis loop shows clearly two distinct polarization states with 180° phase difference, and asymmetric butterfly-shaped loop is observed in the off-field amplitude response. The difference between the two minimum values of the amplitude signal is around 3.75 V and is consistent with the switching voltage of the polarization states. In addition, off-field OOP phase and amplitude hysteresis loops of α-In_2Se_3 nanosheets of 11 nm, 20 nm, 25 nm, 55 nm, and 62 nm thick were also examined and the results are presented in Figure 3.10 (b)-(f).

Similarly, 180° phase switching behaviors and butterfly amplitude loops are identified. In order to validate the precision of the ferroelectric responses, PFM switching spectroscopy measurements were repeated several times at different locations of the same nanoflake and nearly identical signals were received, associated with small variances. These results confirm the presence of robust room-temperature ferroelectric polarization in 2D CVD-fabricated α-In_2Se_3 at different thicknesses.

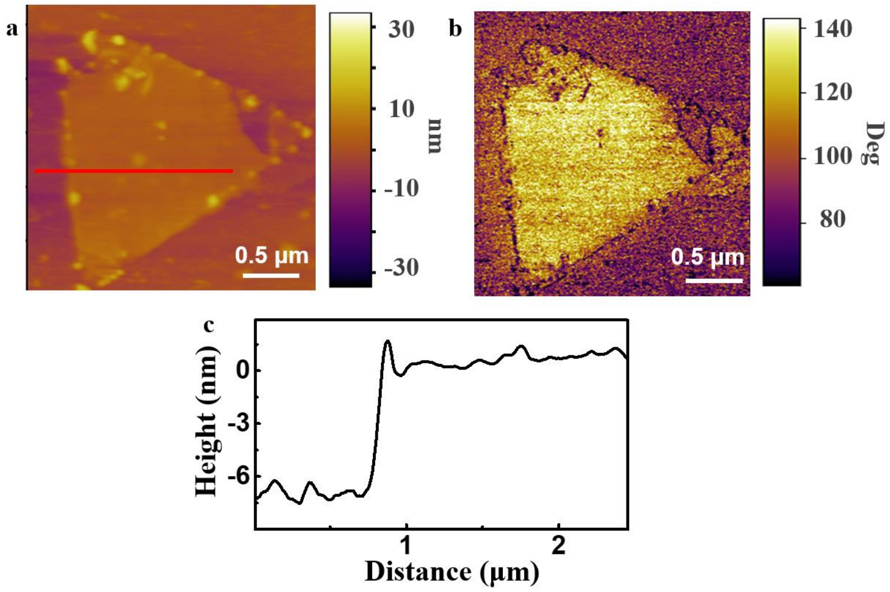

Figure 3.9 Ferroelectric properties of the CVD-grown In_2Se_3 transferred onto Pt/Si substrate. (a) AFM topographic image, (b) PFM OOP phase image and corresponding (c) height profile of a 8 nm In_2Se_3 nanoflake.

Furthermore, the ferroelectric switching characteristics of CVD-grown α-In_2Se_3 were studied in large-scale by modifying the domain pattern of α-In_2Se_3 thin films. Figure 3.11(a) and (b) present the topography and OOP phase images of a 9 nm thick α-In_2Se_3 film after writing two square patterns with opposite tip voltages (+8 V and -7 V). Modified domain pattern with clear phase contrast is observed, demonstrating that polarization direction of the α-In_2Se_3 nanosheets can be switched by the external bias and providing solid evidence for the existence of intrinsic ferroelectricity in 2D α-In_2Se_3.

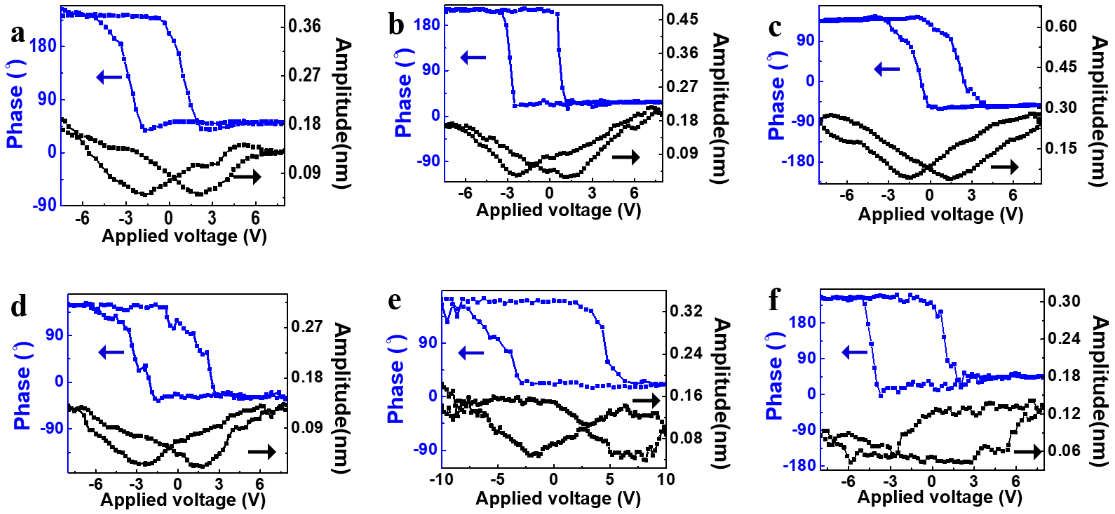

Figure 3.10 Local ferroelectric hysteresis loops of (a) 8 nm, (b) 11nm, (c) 20 nm, (d) 25 nm, (e) 55 nm and (f) 62 nm thick α-In_2Se_3 films.

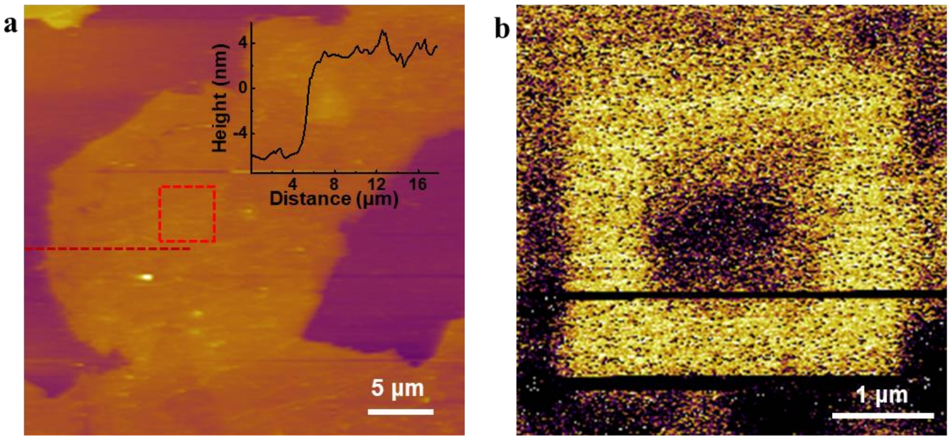

Figure 3.11 (a) Topography of a 9 nm α-In_2Se_3 nanoflake and (b) the corresponding OOP phase image after writing two square patterns sequentially.

3.4.2 Thickness-dependent ferroelectric characterization

In ferroelectric materials, the spontaneous polarization direction is reversible by external electric bias, known as the coercive field (E_c). The coercive field of ferroelectric materials provides essential information for designing practical devices, since the majority of novel electronic devices are demanding a low operating voltage to reduce power consumption. In ferroelectric material-based devices, operating voltage is generally higher than the value of coercive voltage. Hence, investigation of the coercive field for reversing the polarization direction in ferroelectric materials is engaging a high interest. The values of the coercive field were attained by taking the average of multiple measurements of off-field PFM switching loops and were plotted as a function of the layer thickness as presented in Figure 3.12. When the α-In_2Se_3 film thickness is reduced from 62 nm to 8 nm, the coercive field for polarization switching at room-temperature increases from ~0.054 V/nm to ~0.33 V/nm. The coercive field and film thickness are non-linearly related, where the value of coercive field rises rapidly below ~25 nm. When the α-In_2Se_3 nanosheets become thicker, their coercive field gradually decreases due to the weakened depolarization effect, resembling the trend discovered in other conventional ferroelectric materials [103-105].

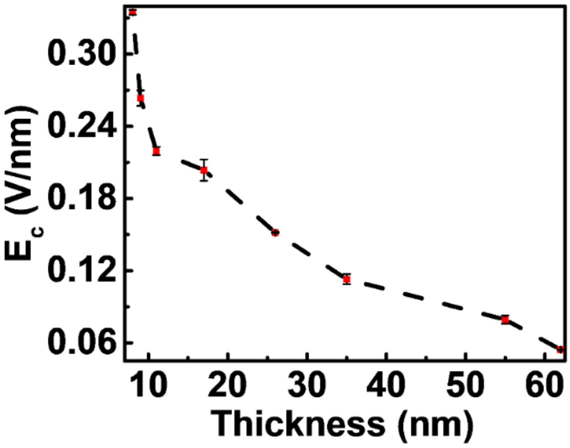

Figure 3.12 Thickness-dependence of coercive field of α-In_2Se_3 thin films.

3.4.3 Temperature-dependent ferroelectric measurements

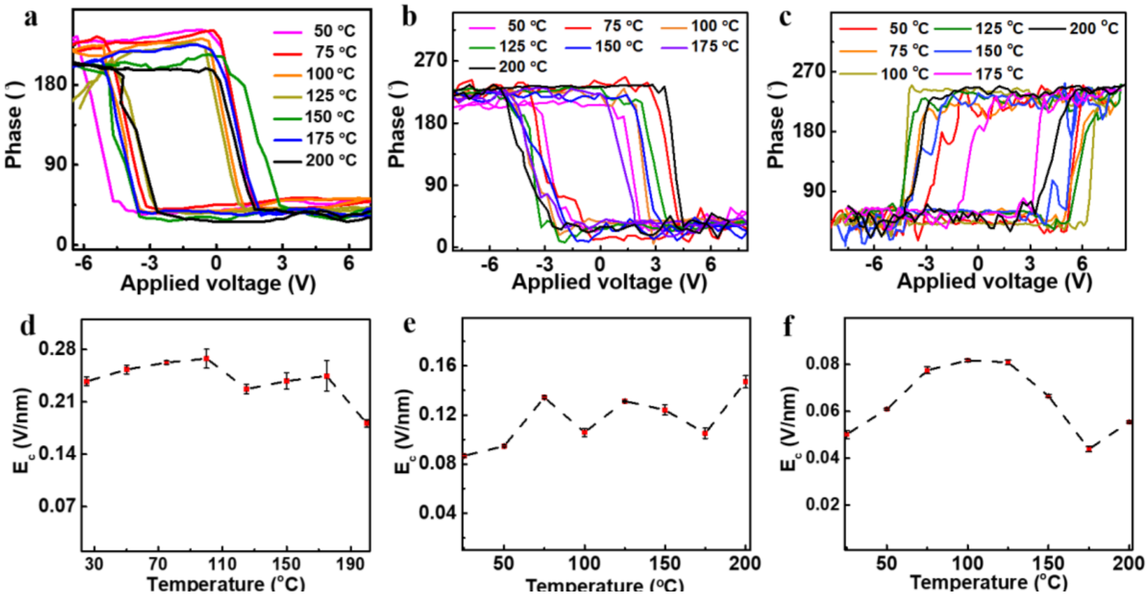

Figure 3.13 PFM phase hysteresis loops of (a) 10 nm, (b) 25 nm and (c) 62 nm α-In_2Se_3 nanosheets at different temperature, and (d-f) their corresponding temperature-dependent coercive fields.

Apart from the robust room-temperature ferroelectricity, 2D α-In_2Se_3 layers possess a relatively high Curie temperature above 200 °C compared to most experimentally reported 2D vdW ferroelectric materials, which further increases when their thickness is reduced. There exists a high potential for 2D α-In_2Se_3 to apply in nanoscale electronic devices working at elevated temperature. In order to examine the high-temperature stability of 2D ferroelectricity in α-In_2Se_3, PFM equipped with a polyheater was used. Switching spectroscopy PFM was conducted locally on α-In_2Se_3 samples (transferred onto Pt substrates) at a wide temperature range from 25 °C to 200 °C. O Figure 3.13(a)-(c) illustrate the off-field OOP hysteresis loops of 10 nm, 25 nm and 62 nm thick In_2Se_3 nanoflakes at various temperature showing clear 180° switching between two polarization states. Moreover, the relationship between temperature and coercive field of In_2Se_3 nanoflakes with the different thicknesses is studied by plotting the coercive field against temperature in Figure 3.13(d)-(f), respectively. There are only small variations in the coercive field of the 10 nm, 25 nm and 62 nm thick In_2Se_3 when temperature increases, and their ferroelectricity can sustain up to 200 °C. The small increase in the coercive field is presumably caused by the clamping effect between the In_2Se_3-substrate interfaces when temperature raised in the range below 100 °C, and probable Se defects on the surface of the α-In_2Se_3 thin films which are investigated by Raman spectroscopy is discussed in next section [106-108]. The OOP phase images of the 25 nm thick In_2Se_3 nanosheet at various temperature are presented in Figure 3.14, in which ferroelectric domain are visualized from 25 °C to 175 °C. When the temperature arrived 200 °C or above, the conductive probe to conduct PFM measurements was not able to work at relatively high temperature and the PFM responses were unstable, causing great difficulty to characterize 2D ferroelectricity above 200 °C. Also, the 25 nm In_2Se_3 nanosheet was damaged during the switching hysteresis loop measurements at 200 °C, as shown in Figure 3.15.

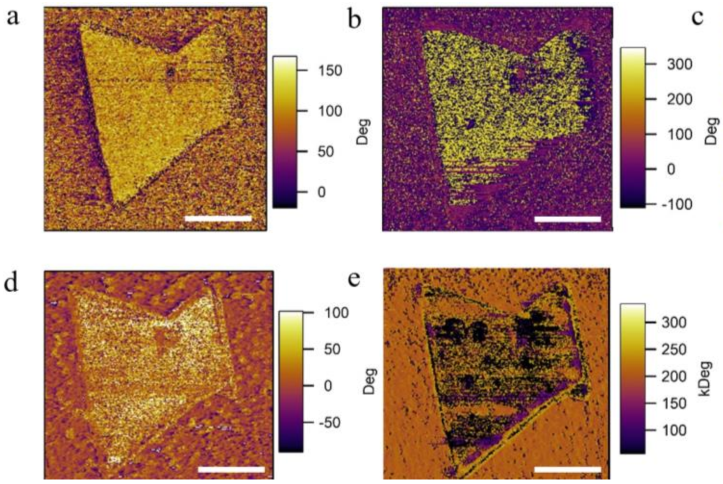

Figure 3.14 OOP phase images of 25 nm thick α-In_2Se_3 nanoflake at (a) 25 °C, (b) 75 °C, (c) 125 °C, (d) 175 °C and (e) 200°C, respectively. Scale bar: 1 μm.

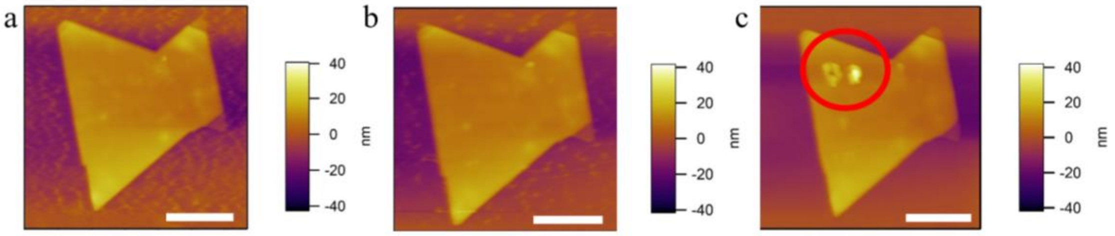

Figure 3.15 Topography of the 25 nm α-In_2Se_3 nanoflake at (a) 25 °C, (b) 175°C and 200 °C, respectively. Scale bar: 1 μm.

On the other hand, the phase of fabricated In_2Se_3 samples after high-temperature PFM characterization was investigated with temperature-variable Raman spectroscopy. Note that only thicker In_2Se_3 nanosheets were tested as ultrathin samples could easily be destroyed even under very low laser power (0.05 mW). Compared with many other 2D materials, the Raman signals of α-In_2Se_3 are relatively weak even with a much longer acquisition time and higher laser power. Also, the Raman peak intensity declines when the thickness of In_2Se_3 films decreases. As shown in Figure 3.16(a) and (b), the α-In_2Se_3 triangle is almost completely damaged after Raman mapping measurement under a low laser power of 0.4 mW. Furthermore, the Raman measurements at higher temperature under the same laser power were more destructive to ultrathin In_2Se_3 samples. Therefore, a low laser power (0.3 mW) was chosen to measure Raman spectra at various temperatures with a reasonable signal-to-noise ratio at the same time avoiding damages to the tested samples. Figure 3.17 presents the Raman spectra from In_2Se_3 nanosheets at the thickness of 16 and 62 nm measured from room temperature to 235 °C. There is no shifting observed from 107 cm^{-1} to 110 cm^{-1} of the A_1 (LO+TO) stretching mode, signifying that there is no α to β phase transformation during measurement, and the CVD-grown In_2Se_3 samples with thickness below 62 nm stably remain in ferroelectric α-phase below 235 °C [109, 110]. In addition to the vibration modes of α-In_2Se_3, there is another peak detected at ~253 cm^{-1} in the 62 nm thick In_2Se_3

which corresponds to the Raman shifting of Se_8 rings [111], suggesting the existence of Se defects on the film surface. The overall Raman measurements have demonstrated 2D α-In_2Se_3 with the merit in robust ferroelectricity at high-temperature environment.

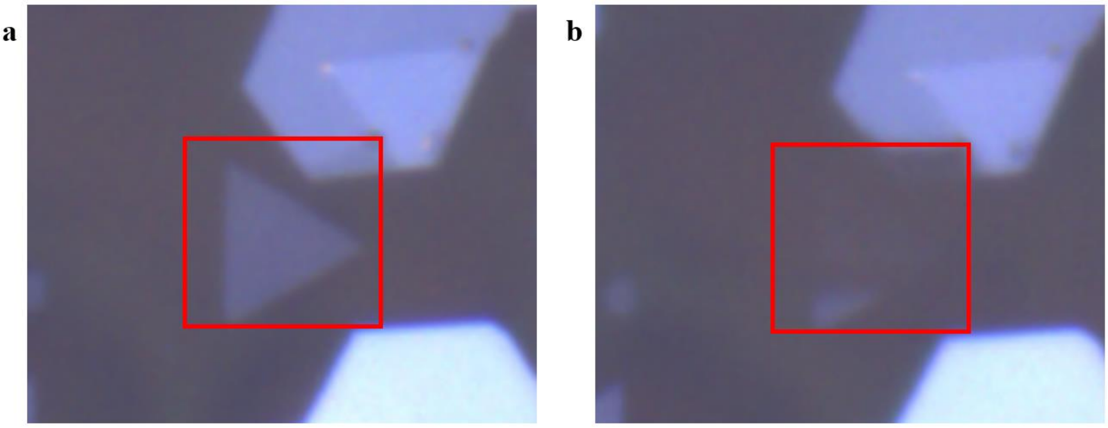

Figure 3.16 Optical images of an In_2Se_3 triangle under Raman characterization. (a) Before and (b) after measurement.

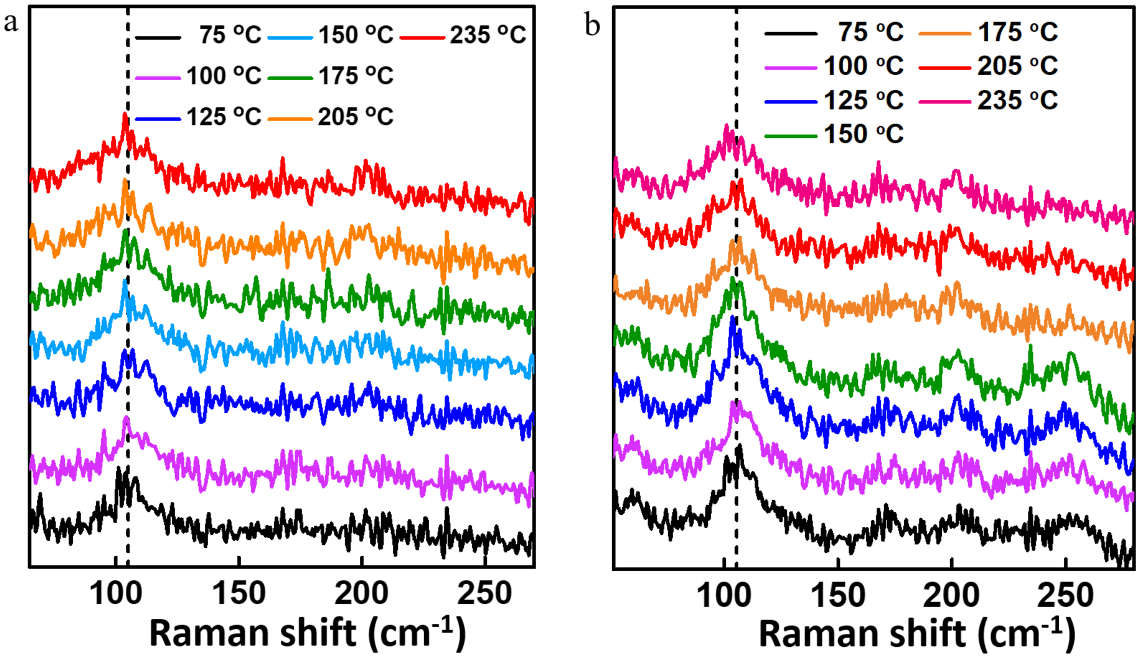

Figure 3.17 Raman spectra of (g) 16 nm and (h) 62 nm In_2Se_3 thin films at various temperature.

As described in the previous session, Curie temperature of the conventional ferroelectric perovskite oxides decreases when they approach the 2D limit. For instance, the transition temperature for bulk $PbTiO_3$, $BaTiO_3$ and $SrTiO_3$ is 490 °C, 120 °C and -270 °C, respectively [112-114]. Even though the intrinsic Curie temperature of several traditional perovskite ferroelectrics is above room temperature, there exists a critical thickness for them to maintain room temperature ferroelectricity which usually around a few to tens of nanometers. When the ferroelectric perovskites are reduced down to nanoscale, their ferroelectricity diminishes at an even lower temperature, largely restricting their usefulness to work at high-temperature environment. On the contrary, the critical temperature of 2D layered ferroelectric materials does not decline with thickness owing to the advantage of the vdW layered structure, making them more promising to apply in high-temperature devices. Nevertheless, the Curie temperature of most 2D layered ferroelectric materials is usually not much higher than room temperature (as indicated in Table 3.1) and they are not suitable to apply in high-temperature electronic devices which generally aiming for a higher operating temperature. Comparatively, 2D α-In_2Se_3 nanosheets are able to retain robust ferroelectricity above 200 °C down to 10 nm thick as illustrated in the present work. This is probably due to the interlocked IP and OOP polarization in α-In_2Se_3 that efficiently stabilizes the ferroelectricity down to single layer at room-temperature, different from the ferroelectric mechanism of other 2D layered ferroelectric materials. Owing to the significantly higher Curie temperature, robust 2D α-In_2Se_3 can be considered as a potential candidate for future nanoscale non-volatile memory devices which good stability at high temperature is desired, especially when placed near other electronic components.

Table 3.2 Comparison of transition temperature of ultrathin films with OOP ferroelectricity.

Materials	**Thickness (nm)**	**Transition temperature T_c (°C)**	**Ref.**
$PbTiO_3$	1.2	RT	[59]
*d*1T-$MoTe_2$	0.8	RT	[83]
WTe_2	1.4	77	[82]
$CuCrP_2S_6$	9	RT	This work
$CuInP_2S_6$	4	42	[86]
2H α-In_2Se_3	1.2	RT	[85]
3R α-In_2Se_3	10	Above 200	This work
RT: room temperature			

3.4.4 Preliminary results of α-In_2Se_3-based heterostructure

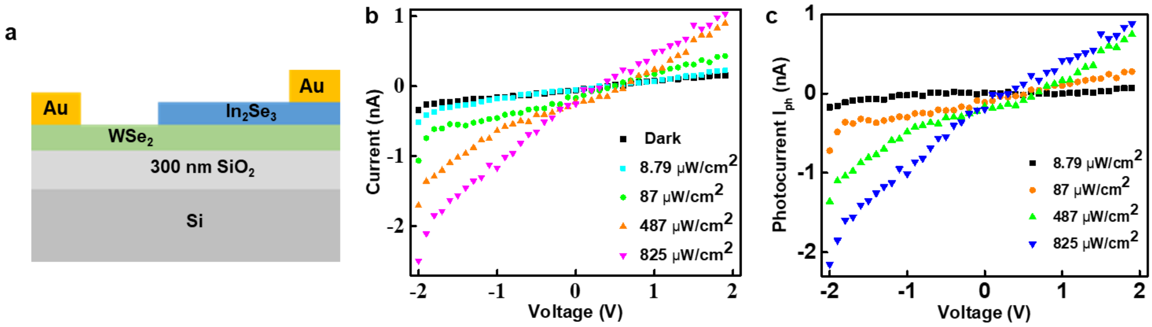

Figure 3.18 Structure and optoelectronic characteristics of WSe_2/In_2Se_3 vdW heterostructure. (a) Schematic diagram of the constructed WSe_2/In_2Se_3 vdW heterostructure. (b) I-V and (c) deduced I_{ph}-V characteristics of the WSe_2/In_2Se_3 heterostructure on SiO_2 substrate under light illumination of 460 nm at different intensity in ambient environment.

Ferroelectric belongs to dielectric materials and is the subset of pyroelectric and piezoelectric materials. Moreover, ferroelectric α-In_2Se_3 also possesses semiconducting and excellent optoelectronic properties. By coupling the different characteristics of α-In_2Se_3, various fascinating and promising device applications can be developed. Herein, a WSe_2/In_2Se_3 vdW heterostructure (Fig. 3.18(a)) was assembled through the dry transfer technique to illustrate the photoresponses of α-In_2Se_3. The fabricated structure formed a p-n junction at the WSe_2/In_2Se_3 interface, affecting the output photocurrent in comparison to a simple In_2Se_3-based device structure. The I-V characteristics of the device were conducted using the probe station with a light source of 460 nm (blue light) at different intensities in an ambient environment and the results were plotted in Figure 3.18(b). The photocurrents I_{ph} were directly calculated from the I-V curves (Fig. 3.18(c)), demonstrating a good photoresponse of the fabricated heterostructure comparable to previously reported work[115]. These preliminary optoelectronic results of the α-In_2Se_3-based heterostructure provides an opportunity to realize the coupling between ferroelectric polarizations and optical properties in the future.

3.5 Summary

In summary, high-quality 2D α-In_2Se_3 nanosheets are successfully fabricated by CVD approach. The morphology and chemical structure are verified using optical microscopy, Raman spectroscopy, XPS, AFM and TEM techniques. Robust vertical ferroelectricity of α-In_2Se_3 down to 10 nm thick are further examined experimentally from room temperature to high temperature range. The ferroelectric phase switching behaviors and ferroelectric domains of In_2Se_3 from room temperature to high temperature (up to 200 °C) were illustrated by PFM, demonstrating their intrinsic high transition temperature. Additionally, the coercive field for reversing the polarization direction rises substantially when the In_2Se_3 films become thinner, and there is no obvious variation in the coercive field when the temperature increases. The findings can extend the functionalities of 2D α-In_2Se_3 and provide essential insights into promising high-temperature nanoelectronic applications on the basis of In_2Se_3 and other 2D ferroelectric materials.

Chapter 4 Ferroelectric Properties of Few-Layer ABP_2X_6 Nanoflakes

4.1 Introduction

Recently, ultrathin transition metal thiophosphates (TMTP) with the structure of ABP_2X_6 (A = Ag, Cu; B = Bi, In; X = S, Se) are receiving considerable attention as they can potentially retain ferroelectricity in ultrathin layers [116]. Various members of TMTP family are predicted the existence of OOP ferroelectricity in 2D limits including $AgBiP_2Se_6$ and $CuBiP_2Se_6$ via first-principles calculations [74, 75]. Especially, $CuInP_2S_6$ (CIPS) is demonstrated experimentally to exhibit stable OOP ferroelectric polarization in atomically thin layers at room temperature [81, 117]. CIPS is a ferrielectric system with a critical temperature at ~42 °C [100]. For simplicity, as ferrielectric materials exist identical characteristics as ferroelectric materials, which are the presence of spontaneous electric polarization that is reversible by external electric field, CIPS is referred as ferroelectrics as well. On the other hand, $CuCrP_2S_6$ (CCPS) is a multiferroic material which has been proposed to possess room-temperature ferroelectricity in single-layer and few-layers in theory by Lai and his coworkers [87]. Lai *et al.* also report with experiments the discovery of OOP ferroelectricity in ~13 nm thick CCPS nanoflake at room temperature. However, the ferroelectric properties of atomically thin CCPS nanoflakes have not been extensively explored and still, limited experimental observations are provided so far. In this chapter, the structure and crystal quality of CIPS and CCPS are examined by Raman spectroscopy, SHG, XRD, TEM and EDX techniques. We also demonstrate experimentally the switchable OOP ferroelectric polarization of ultrathin CIPS and CCPS films with thickness below 10 nm via PFM, promoting new candidates for developing ferroelectric devices in the 2D nanoscale electronic field.

4.2 Fabrication and structural characterization of $CuInP_2S_6$ nanoflakes

For Raman measurements and ferroelectric characterization, atomically thin CIPS nanosheets were prepared through mechanical exfoliation via Scotch tape onto conductive Pt substrates. For TEM analysis, CIPS nanoflakes were fabricated by liquid-phase exfoliation method onto TEM grid. In the liquid-phase exfoliation approach, bulk CIPS crystal was dispersed in a mixture of water and ethanol (ratio 1:1) and treated with ultrasound operating at 120 W for 3 hrs. After sonication, the resulting dispersion was centrifuged at 1000 rpm for 5 min to extract supernatant containing ultrathin CIPS nanosheets. The collected supernatant was centrifuged at 10,000 rpm for another 5 min to precipitate the nanosheets. Finally, the obtained CIPS nanosheets were transferred onto the TEM grid by micropipette.

4.2.1 Raman and characterization

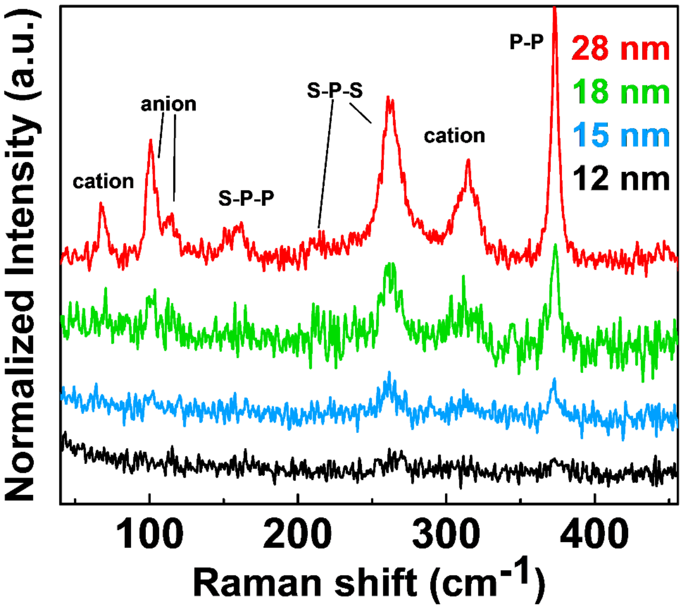

Figure 4.1 Raman spectra of CIPS nanoflakes with thickness from 12 nm to 28 nm by using 532 nm excitation laser.

The crystal structure was identified via Witec confocal Raman spectroscopy equipped with an excitation laser with 532 nm wavelength. The accurate thickness of several CIPS nanoflakes was first characterized using AFM operating in tapping mode. Raman spectra of CIPS nanosheets with different thicknesses from 12 to 28 nm were measured and are displayed in Figure 4.1. The Raman characteristics of the exfoliated CIPS nanosheets at various thickness are identical and are consistent with the reported Raman shifting of bulk CIPS crystal at ferroelectric phase [100]. The broad peaks in the 60-80 and 300-325 cm^{-1} ranges are ascribed to cation (Cu^{+}, In^{3+}) vibration modes, and that in 90-120 cm^{-1} range is attributed to anion ($P_2S_6^{4-}$) vibration modes. Numerous peaks in the 145-285 cm^{-1} range correspond to S-P-P and S-P-S oscillation modes, and P-P stretching is responsible for the sharp peak at ~375 cm^{-1}.

4.2.2 Structural measurements

Through SHIM, the non-centrosymmetric structure of CIPS samples was verified and the SHG spectrum is displayed in Figure 4.2(a). In the single-crystal XRD spectrum (Figure 4.2(b)) collected at room temperature, there are two strong and sharp peaks at 13.9 and 27.8 were assigned to [002] and [004], in good agreement with the reported CIPS crystal in ferrielectric phase. Figure 4.2(c) demonstrates the lattice structure of CIPS from top and side views, which is based on periodic hexagonal sulfur rings with triangular P-P pairs and Cu, In atoms centering at the rings. CIPS layers are stacked vertically by weak vdW interactions. The crystal structure in the atomic scale and crystallinity of CIPS samples were characterized using TEM equipped with EDX. Figure 4.2 (d) displays the HRTEM image of the top view of CIPS nanosheet showing uniform and periodic crystal lattices in the same orientation. Also, the corresponding SAED as shown in the inset of Figure 4.2(d) demonstrates several sets of rotational symmetry patterns with a perfect hexagonal structure, indicating that the CIPS nanoflakes are and single-crystallized in high quality. Besides, the elemental composition of the CIPS films on the copper grid was detected by EDX and the X-ray energy spectrum and elemental mappings are presented in Figure 4.3. Characteristic X-rays of all four elements existing in CIPS (Cu^+, In^{3+}, P^{4+} and S^{2-}) are detected, further confirming the chemical composition of the measured CIPS samples.

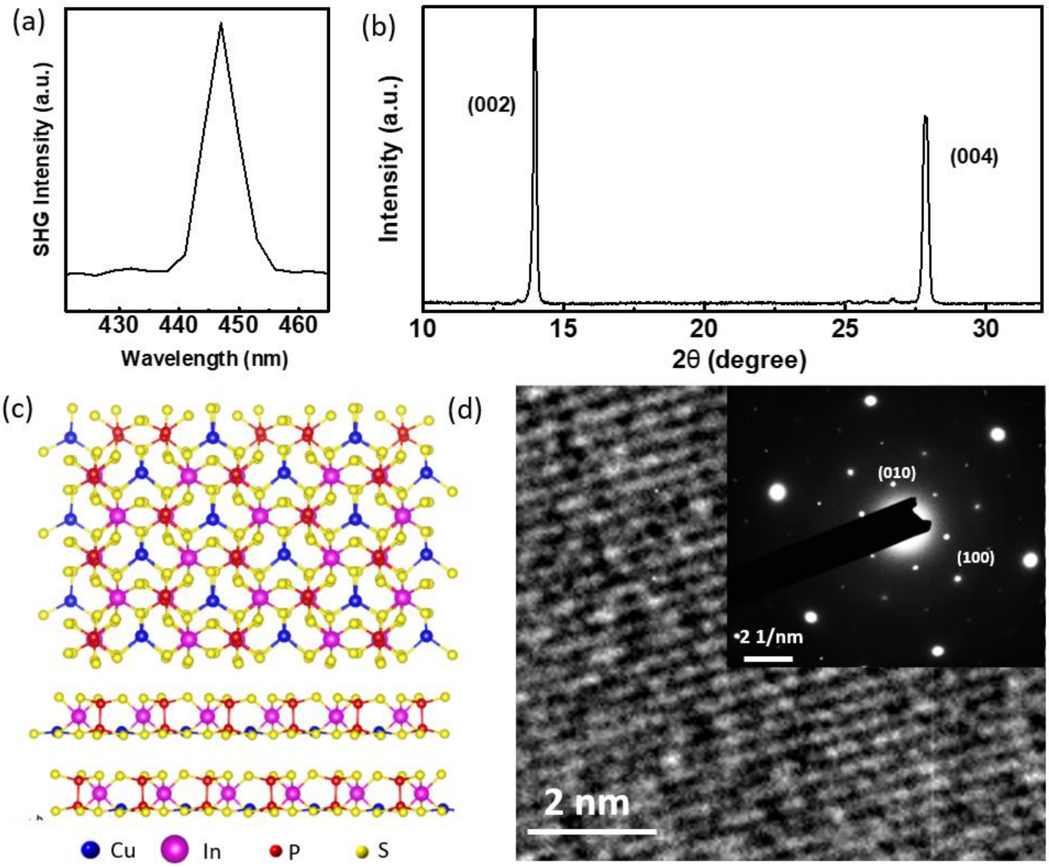

Figure 4.2 (a) SHG response of CIPS samples at room temperature, with an excitation laser wavelength of 900 nm. (b) Typical XRD spectrum of CIPS at T = 298 K and ambient conditions. (c) The top-view and side-view for the crystal structure of CIPS and (d) HRTEM image of exfoliated CIPS nanoflakes, inset: corresponding SAED pattern.

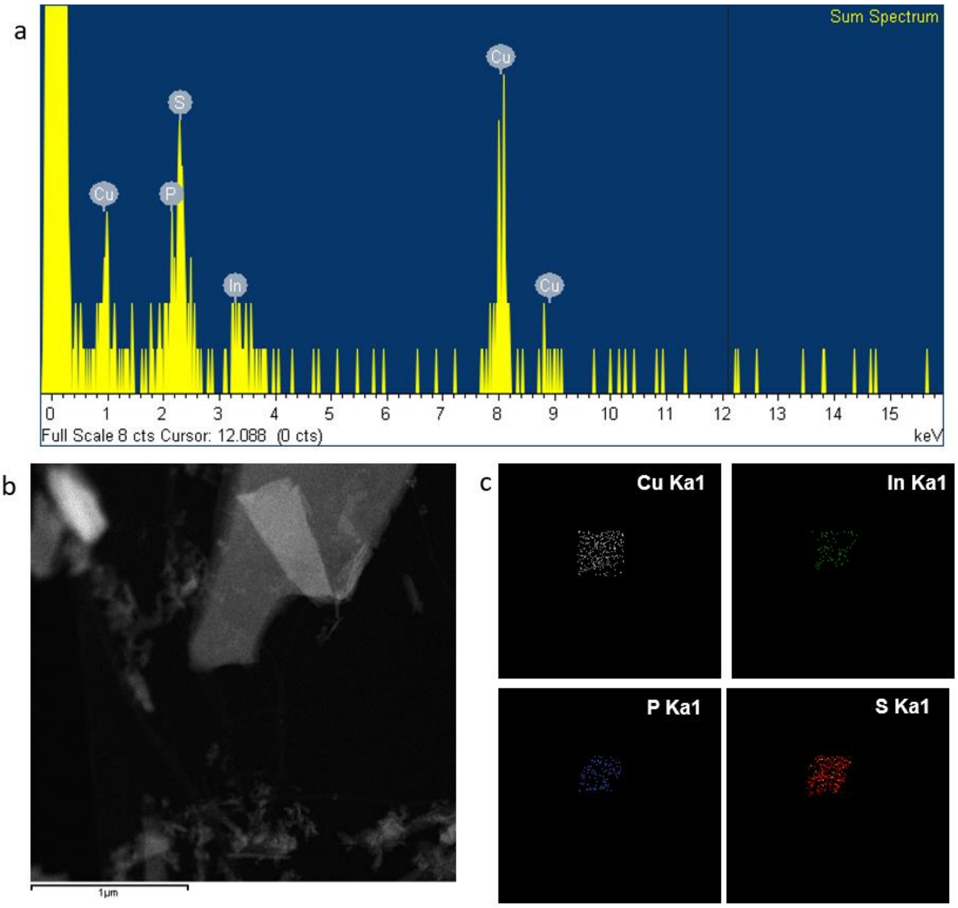

Figure 4.3 (a) EDX elemental analysis, (b) image and (c) elemental mapping of exfoliated CIPS sample.

4.3 Room-temperature ferroelectricity in $CuInP_2S_6$ nanoflakes

Different from the mechanism of In_2Se_3, the internal spontaneous polarization in CIPS arises from the off-centering displacements of Cu^+ and In^{3+} ions in opposite directions. Their displacements are anti-parallel and unequal and Cu^+ ions contribute more polarization to compensate for the polarization by In^{3+} ions, resulting in a net polarization field and is large enough to be detected. PFM was conducted to characterize the vertical ferroelectric polarization in ultrathin layered CIPS nanoflakes at room temperature. As displayed in Figure 4.4, ferroelectric domains can be clearly visualized in 5-12 nm thick CIPS samples exfoliated on Pt substrates. Figure 4.5 reveals the topography and OOP polarization switching behaviors of CIPS samples of 9 nm, 14.4 nm and 24 nm thick. The off-field local phase hysteresis loops show clear switching between two polarization states with 180° phase difference, and asymmetric butterfly-shaped loops are detected in the off-field amplitude signals. The amplitude of the piezoelectric response increases with the increase in thickness of the measured nanosheets. Both the 180° phase reversal and butterfly amplitude loop essentially verify the room-temperature ferroelectricity in CIPS nanosheets down to 9 nm thick.

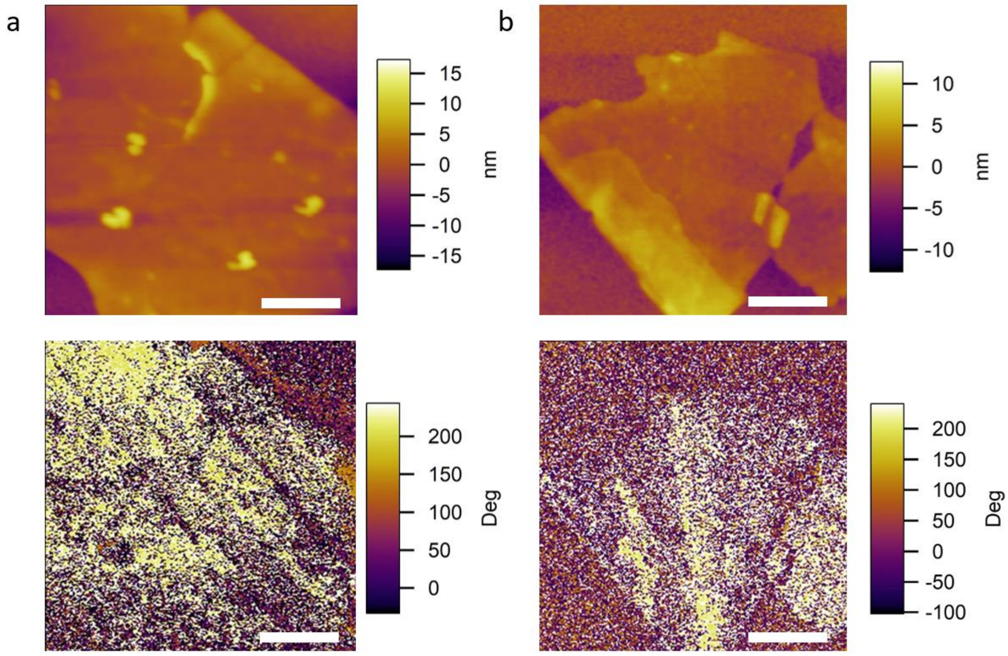

Figure 4.4 Topography and PFM phase images showing clear ferroelectric domains in (a) 12 nm and (b) 5-9 nm thick CIPS nanoflakes. Scale bar: 0.5 nm.

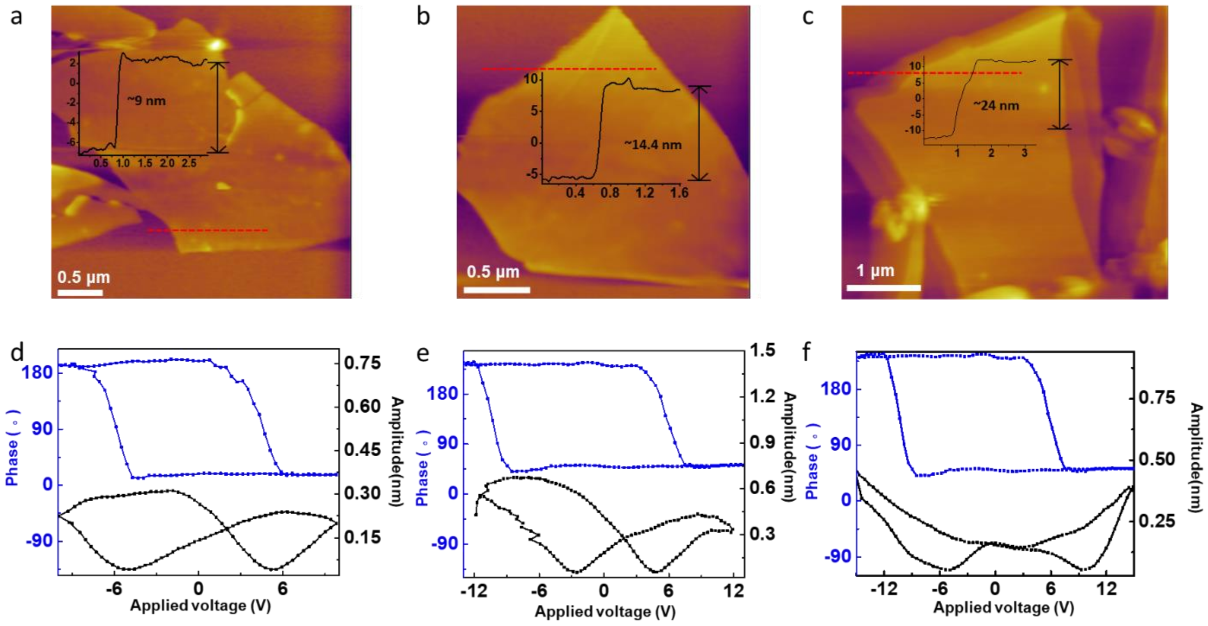

Figure 4.5 (a-c) Topography images and height profiles, and (d-f) corresponding OOP ferroelectric hysteresis loops of CIPS nanoflakes with different thicknesses of 9 nm, 14.4 nm and 24 nm, respectively.

4.4 Structural measurements of exfoliated ultrathin CuCrP$_2$S$_6$ layers

CCPS nanosheets were fabricated onto arbitrary substrates through similar approaches as CIPS by mechanical cleavage or liquid-phase exfoliation for later characterizations.

4.4.1 Optical characterization

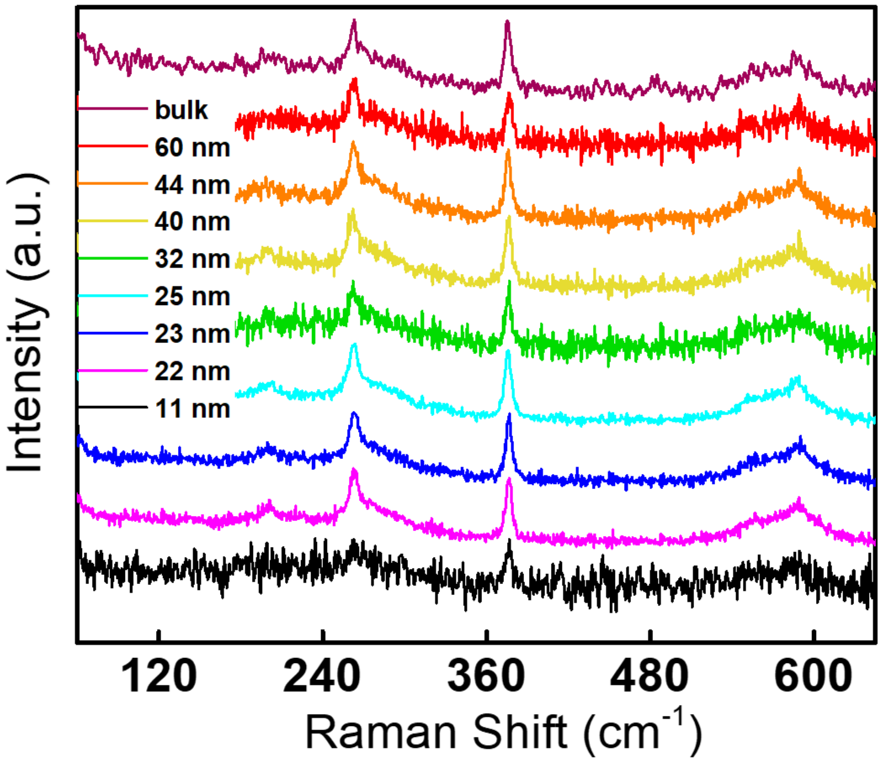

Figure 4.6 Raman spectra of CCPS nanoflakes with thickness from 11 nm to bulk crystal with 532 nm excitation laser.

The exfoliated CCPS nanosheets were inspected with Witec confocal Raman spectroscopy equipped with an excitation laser of 532 nm wavelength. The precise thickness of various CCPS nanosheets was first obtained by AFM technique. Figure 4.6 presents the plotted Raman spectra of 2D CCPS nanosheets at a range of thickness from 11 to bulk samples. The locations of Raman peaks of the exfoliated CCPS samples at different thicknesses are identical, and the two dominant peaks at ~261 and 376 cm^{-1} are attributed to the S-P-S and P-P vibration modes.

4.4.2 Structural characterization

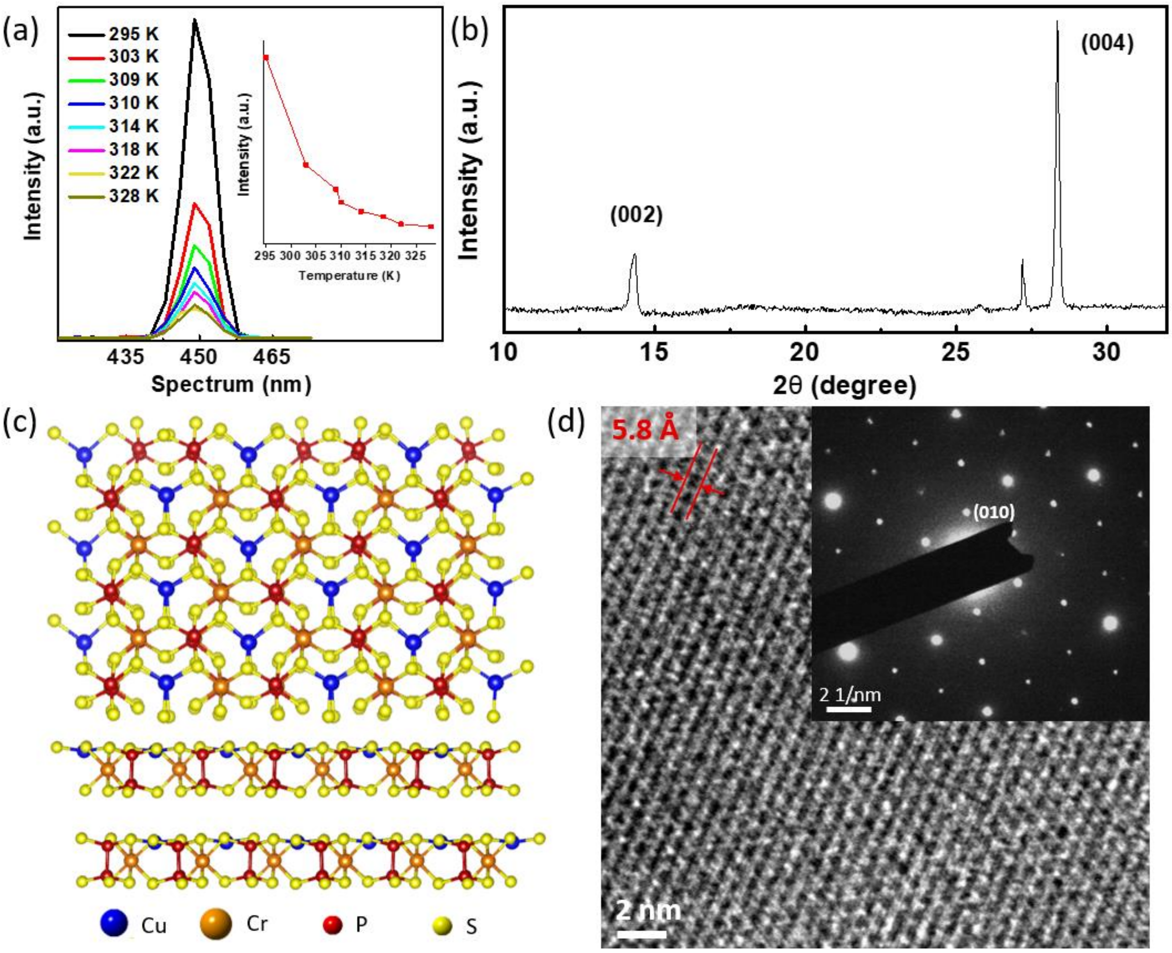

Figure 4.7 (a) SHG spectrum of CCPS samples with an excitation laser wavelength of 900 nm. (b) XRD pattern of CCPS crystal at room temperature. (c) Top-view and side-view for the crystal of CCPS crystal and (d) HRTEM image of CCPS nanosheet, inset: corresponding SAED pattern.

The SHG responses in Figure 4.7(a) indicate the non-centrosymmetric structure of the exfoliated CCPS samples, and the intensity of the SHG signals gradually declines with the increase in temperature. XRD analysis was performed to further confirm the structure of CCPS crystal and the XRD pattern is depicted in Figure 4.7 (b). The set of strong peaks at ~14.3 and 28.3 are attributed to [002] and [004], consistent with the reported values of CCPS crystals in ferroelectric phase. CCPS has a crystal structure similar to CIPS, and the top- and side-view are shown in Figure 4.7 (c). The crystal structure of CCPS consists of a hexagonal sulfur framework filled by Cu, Cr and P-P triangular patterns. Since each CCPS layer is connected via weak vdW interactions, ultrathin nanoflakes are possible to be exfoliated from bulk CCPS. The structure and lattice orientation of CCPS nanoflakes were observed using TEM. As shown in Figure 4.7(d), the HRTEM image of the top-view illustrates a periodic hexagonal structure along identical orientation and the lattice spacing for the (100) planes is measured to be ~5.8 Å. The inset corresponding SAED pattern also demonstrates discrete diffraction spots with 6-fold rotational symmetry, verifying the CCPS samples are highly single-crystalline. In addition, the elemental composition of CCPS was analyzed by EDX and the resulting energy spectrum and elemental mappings are presented in Figure 4.8. Characteristic X-rays of Cu, Cr, P and S elements are collected, further confirming the chemical composition of CCPS samples used in this work.

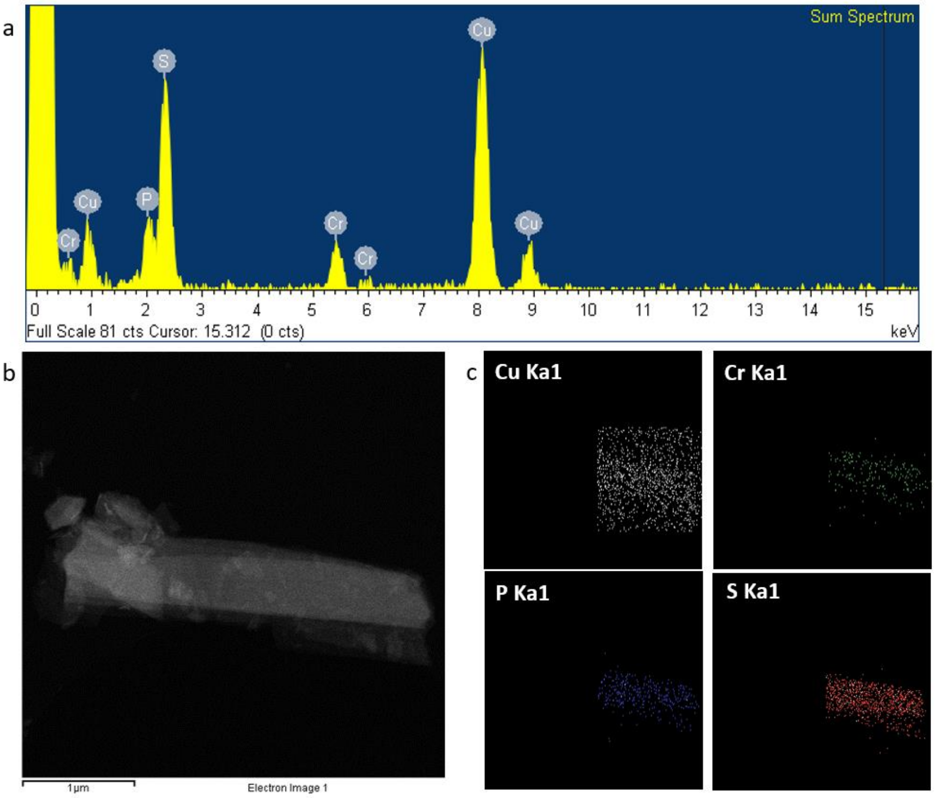

Figure 4.8 (a) EDX elemental analysis, (b) image and (c) elemental mapping of CCPS nanoflakes.

4.5 Room-temperature ferroelectricity in layered $CuCrP_2S_6$ nanosheets

Unlike CIPS, the ferroelectricity from CCPS is contributed only from the off-centering Cu atoms. In the ideal ferroelectric phase of CCPS, the Cu atoms lay on the same side of each CCPS layer (see Figure 4.7(c)), leading to a net vertical electric polarization field. PFM is a very powerful equipment for the observation of switchable electric polarization in ultrathin 2D ferroelectric materials. Discrete ferroelectric domains of CCPS samples are shown in Figure 4.9, and no domain contrast is observable in the PFM phase image of CCPS nanoflakes with various thickness (Figure 4.9(b)), demonstrating that CCPS samples with different thicknesses tend to form a single domain in the same direction. Figure 4.10 illustrates the single-point switching PFM phase and amplitude hysteresis loops measured from ultrathin CCPS flakes down to ~6 nm and 9 nm thick. Two distinct polarization states are achieved with a phase difference of 180° and the coercive voltages coincide with the difference in two minima of the amplitude signals. These results resemble to typical ferroelectric responses and demonstrate that OOP ferroelectricity in 2D CCPS nanoflakes at room temperature can be sustainable down to 6 nm. The room-temperature ferroelectricity in ultrathin CCPS was further demonstrated in large-scale by modifying the polarization direction of a 9 nm thick CCPS flake through writing two square patterns with opposite tip voltages (+12 V and -12 V). The topography and height profile of the characterized flake is displayed in Figure 4.11(a). After modifying the polarization states, OOP amplitude and phase images were measured as presented in Figure 4.11(b) and (c) respectively. The clear PFM amplitude and phase contrasts signify the existence of room-temperature OOP ferroelectricity in CCPS with a thickness of 9 nm.

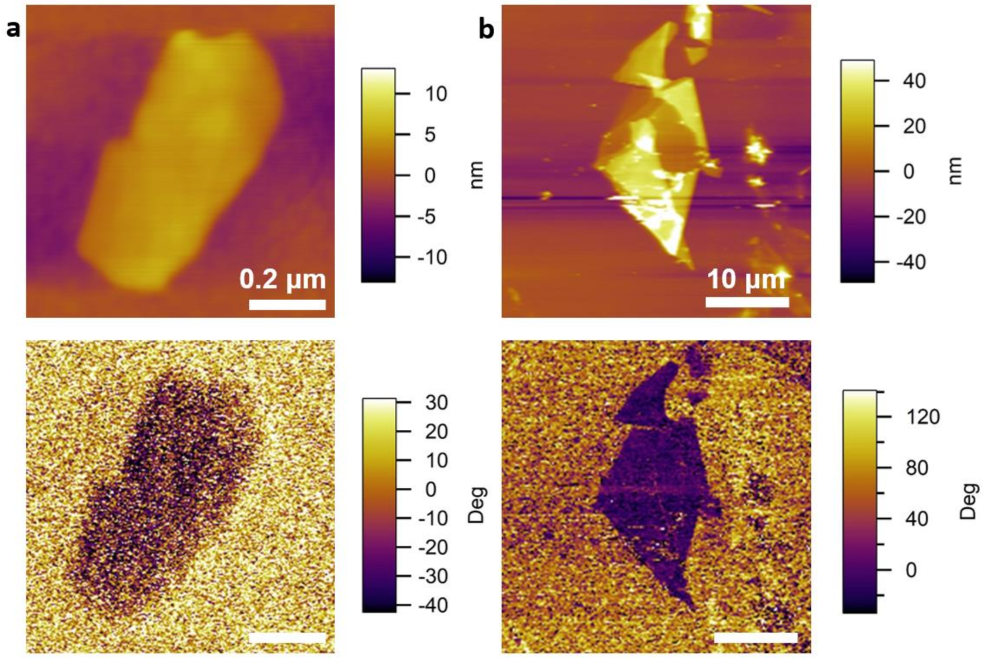

Figure 4.9 (a-b) Topography and PFM phase images with clear ferroelectric domains in (a) 12 nm and (b) 5-49 nm thick CIPS nanoflakes.

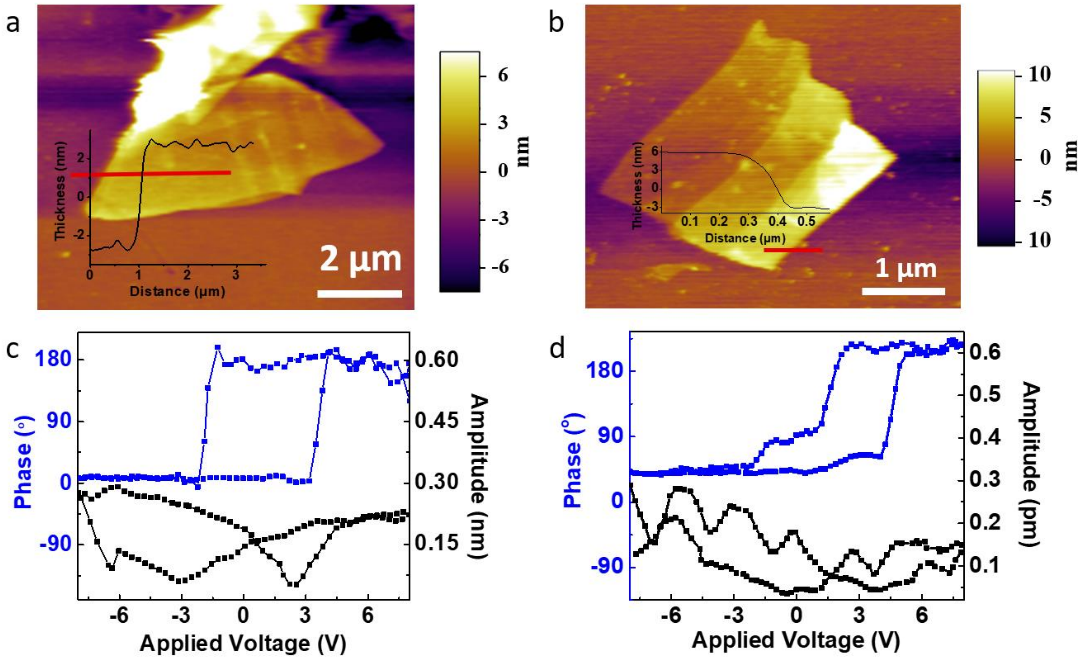

Figure 4.10 (a-b) Topography images and height profiles, and (c-d) corresponding OOP ferroelectric hysteresis loops of 6 nm and 9 nm thick CCPS nanoflakes.

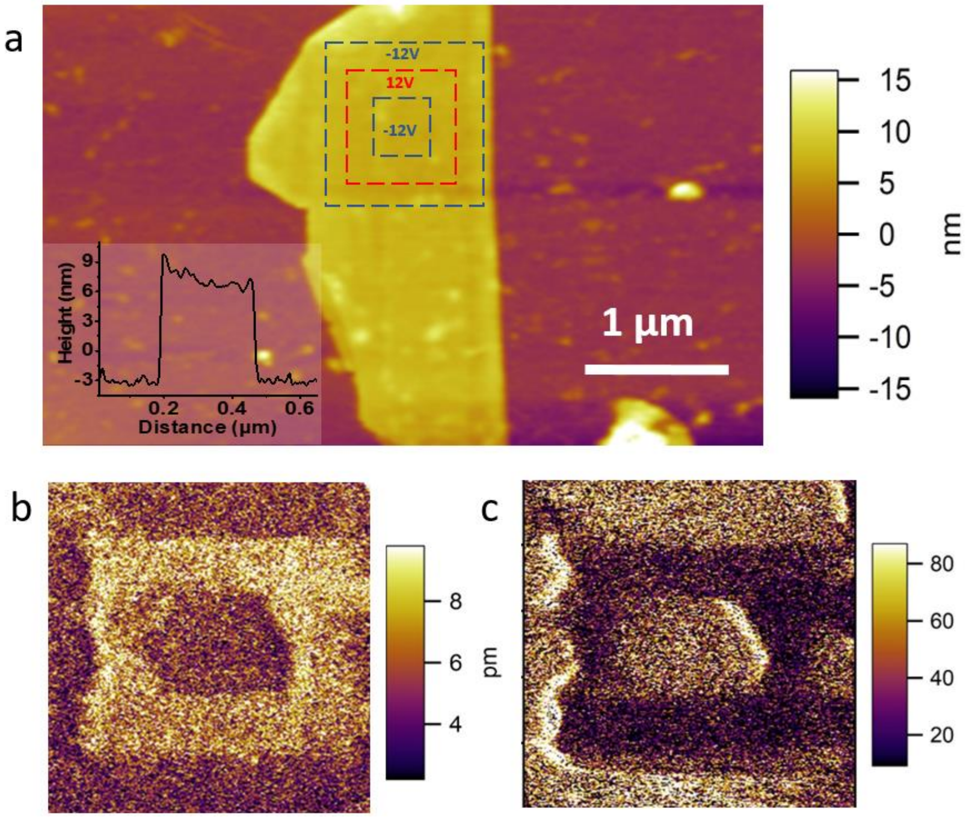

Figure 4.11 (a) Topography and height profile of a 9 nm CCPS film exfoliated on Pt substrate and (b-c) the OOP amplitude and phase images after writing two square patterns sequentially.

4.6 Summary

In this chapter, lattice structures of CIPS and CCPS crystals were analyzed by Raman spectroscopy SHG microscopy and TEM equipped with EDX. 2D CIPS and CCPS nanosheets with various thicknesses are maintained in the ferroelectric phase at room temperature as confirmed by Raman spectra. Furthermore, the ferroelectric phenomena in vertical direction of CIPS and CCPS are observed using PFM, and the switchable ferroelectric polarization can sustain down to 9 nm and 6 nm in CIPS and

CCPS, respectively. This study of intrinsic 2D ferroelectricity in CIPS and CCPS offers new alternatives for developing novel nanoelectronic devices based on atomically thin ferroelectric materials.

Chapter 5 Conclusions and Future Prospects

5.1 Conclusions

Ultrathin ferroelectric materials which possess outstanding electrical and optical properties have drawn enormous research interest in the field of nanoelectronics and optoelectronics, including transistors, actuators, photovoltaics, optical sensors, ferroelectric analog synapses, and non-volatile memory devices. Nonetheless, there exhibits an intrinsic size effect in conventional ferroelectric perovskites which significantly degrades their strength of ferroelectric polarization and transition temperature in the 2D limit, and their ferroelectricity will vanish below a critical thickness, usually about tens of nanometers. To date, ferroelectricity has been theoretically predicted in a variety of novel 2D layered materials, but experimental discoveries still remain scarce. Moreover, Curie temperature of the reported 2D vdW ferroelectric materials is usually quite low or simply above room temperature, limiting their applications to operate in high-temperature environment. The details of the thesis are summarized below.

Firstly, α-In_2Se_3 is chosen among various 2D ferroelectric materials owing to its ultrahigh ferroelectric transition temperature, and high-quality α-In_2Se_3 nanosheets were fabricated by CVD method at atmospheric pressure. We demonstrate the room-temperature ferroelectric and piezoelectric responses in 2D α-In_2Se_3 samples with different thicknesses. When the thickness of In_2Se_3 films reduces from 62 nm to 8 nm, the coercive field contributing to polarization state switching drastically increases from 0.054 V/nm to 0.33 V/nm. Furthermore, robust high-temperature ferroelectricity is illustrated in CVD-grown α-In_2Se_3 nanosheets down to 10 nm with stable OOP spontaneous polarization maintained above 200 °C. Polarization switching behaviors and ferroelectric domains are observed experimentally in ultrathin In_2Se_3 films from room temperature to high temperature. At different temperatures, there is no large variance identified in the coercive field value of In_2Se_3 nanosheets with identical thickness. Our results sufficiently provide evidence of the intrinsic high Curie temperature of α-In_2Se_3 much higher than room temperature and open up possibilities for developing novel high-temperature nanoelectronic devices based on α-In_2Se_3 as well as other 2D ferroelectrics.

Secondly, we report the existence of vertical ferroelectricity in two layered TMTP materials including CIPS and CCPS and indicate their ferroelectric mechanisms. Their structures are verified by Raman spectroscopy SHIG, XRD and TEM techniques. Single ferroelectric domain in OOP direction is clearly visualized and switching behaviors of ferroelectric polarization are observed in both materials by PFM. The OOP ferroelectricity is intrinsically stable against depolarization field at room temperature down to 9 nm and 6 nm in CIPS and CCPS nanoflakes, respectively. Our findings verify the previous theoretical calculations and promote the development of functional electronics at nanoscale.

5.2 Future prospects

The excellent thermal stability of ferroelectricity in 2D α-In_2Se_3 crystal is sufficiently demonstrated in this work and provides an alternative approach to utilize ferroelectric materials at high-temperature environment. Besides spontaneous electric polarization, ferroelectric materials also exhibit many other characteristics such as semiconducting, piezoelectric and pyroelectric effect. By leveraging different electric properties, new physical phenomena can be realized through the construction of various vdW heterostructures with the combination of 2D vdW ferroelectrics and other functional materials. In the future, we can fabricate various functional devices based on high-quality large-scale CVD-grown α-In_2Se_3 and investigate their performance for use in the high-temperature fields. For example, energy harvesting devices based on the pyroelectric effect and high-temperature sensors can be explored and the functionalities of 2D ferroelectric materials can be enriched.

On the other hand, the thinnest possible thicknesses of CIPS and CCPS that still preserve ferroelectric characteristics have not been achieved in experiments. With further thickness reduction of the CIPS and CCPS nanoflakes, it is probable for ferroelectricity in TMTP materials to be survived down to monolayer limit which is highly desirable for non-volatile memory and other nanoscale electronic devices. More importantly, the stabilization of polarization in these 2D ferroelectric materials which is a major consideration for their applications is not fully studied. Long-term PFM and TEM analysis can be conducted for further *in-situ* characterization on the ferroelectric domains and phase transition of 2D vdW ferroelectric materials.

References

[1] Novoselov, K. S.; Geim, A. K.; Morozov, S. V.; Jiang, D.; Zhang, Y.; Dubonos, S. V.; Grigorieva, I. V.; Firsov, A. A. Electric Field Effect in Atomically Thin Carbon Films. *Science* **2004**, 306, 666-669.

[2] Changgu, L.; Xiaoding, W.; Jeffrey, W. K.; James, H. Measurement of the Elastic Properties and Intrinsic Strength of Monolayer Graphene. *Science* **2008**, 321, 385-388.

[3] Balandin, A. A.; Ghosh, S.; Bao, W.; Calizo, I.; Teweldebrhan, D.; Miao, F.; Lau, C. N. Superior Thermal Conductivity of Single-Layer Graphene. *Nano Lett.* **2008**, 8, 902-907.

[4] Nair, R. R.; Blake, P.; Grigorenko, A. N.; Novoselov, K. S.; Booth, T. J.; Stauber, T.; Peres, N. M. R.; Geim, A. K. Fine Structure Constant Defines Visual Transparency of Graphene. *Science* **2008**, 320, 1308-1308.

[5] Chen, Z.; Lin, Y.-M.; Rooks, M. J.; Avouris, P. Graphene Nano-Ribbon Electronics. *Physica E Low Dimens. Syst. Nanostruct.* **2007**, 40, 228-232.

[6] Bonaccorso, F.; Hasan, T.; Sun, Z.; Ferrari, A. C. Graphene Photonics and Optoelectronics. *Nat. Photonics* **2010**, 4, 611-622.

[7] Lin, Y.-m.; Xia, F.; Valdes-Garcia, A.; Mueller, T.; Avouris, P. Ultrafast Graphene Photodetector. *Nat. Nanotechnol.* **2009**, 4, 839-843.

[8] Bolotin, K. I.; Sikes, K. J.; Jiang, Z.; Klima, M.; Fudenberg, G.; Hone, J.; Kim, P.; Stormer, H. L. Ultrahigh Electron Mobility in Suspended Graphene. *Solid State Commun.* **2008**, 146, 351-355.

[9] Wang, Q. H.; Kalantar-Zadeh, K.; Kis, A.; Coleman, J. N.; Strano, M. S. Electronics and Optoelectronics of Two-Dimensional Transition Metal Dichalcogenides. *Nat. Nanotechnol.* **2012**, 7, 699-712.

[10] Jariwala, D.; Sangwan, V. K.; Lauhon, L. J.; Marks, T. J.; Hersam, M. C. Emerging Device Applications for Semiconducting Two-Dimensional Transition Metal Dichalcogenides. *ACS Nano* **2014**, 8, 1102-1120.

[11] Li, W.; Li, J. Ferroelasticity and Domain Physics in Two-Dimensional Transition Metal Dichalcogenide Monolayers. *Nat. Commun.* **2016**, 7, 10843.

[12] Xiaofeng, Q.; Junwei, L.; Liang, F.; Ju, L. Quantum Spin Hall Effect in Two-Dimensional Transition Metal Dichalcogenides. *Science* **2014**, 346, 1344-1347.

[13] Xu, X.; Yao, W.; Xiao, D.; Heinz, T. F. Spin and Pseudospins in Layered Transition Metal Dichalcogenides. *Nat. Phys.* **2014**, 10, 343-350.

[14] Sun, Z.; Liao, T.; Dou, Y.; Hwang, S. M.; Park, M.-S.; Jiang, L.; Kim, J. H.;

Dou, S. X. Generalized Self-Assembly of Scalable Two-Dimensional Transition Metal Oxide Nanosheets. *Nat. Commun.* **2014**, 5, 3813.

[15] Zavabeti, A.; Ou, J. Z.; Carey, B. J.; Syed, N.; Orrell-Trigg, R.; Mayes, E. L. H.; Xu, C.; Kavehei, O.; apos; Mullane, A. P.; Kaner, R. B.; Kalantar-Zadeh, K.; Daeneke, T. A Liquid Metal Reaction Environment for the Room-Temperature Synthesis of Atomically Thin Metal Oxide. *Science* **2017**, 358, 332-335.

[16] Kalantar-zadeh, K.; Ou, J. Z.; Daeneke, T.; Mitchell, A.; Sasaki, T.; Fuhrer, M. S. Two Dimensional and Layered Transition Metal Oxides. *Appl. Mater. Today* **2016**, 5, 73-89.

[17] Lv, L.; Yang, Z.; Chen, K.; Wang, C.; Xiong, Y. 2D Layered Double Hydroxides for Oxygen Evolution Reaction: From Fundamental Design to Application. *Adv. Energy Mater.* **2019**, 9, 1803358-n/a.

[18] Shao, M.; Zhang, R.; Li, Z.; Wei, M.; Evans, D. G.; Duan, X. Layered Double Hydroxides toward Electrochemical Energy Storage and Conversion: Design, Synthesis and Applications. *Chem. Commun.* **2015**, 51, 1588-15893.

[19] Luo, Z.; Maassen, J.; Deng, Y.; Du, Y.; Garrelts, R. P.; Lundstrom, M. S.; Ye, P. D.; Xu, X. Anisotropic In-Plane Thermal Conductivity Observed in Few-Layer Black Phosphorus

Nat. Commun. **2015**, 6, 8572.

[20] Smith, J. B.; Hagaman, D.; Ji, H.-F. Growth of 2D Black Phosphorus

Film from Chemical Vapor Deposition. *Nanotechnology* **2016**, 27, 215602.

[21] Castellanos-Gomez, A.; Vicarelli, L.; Prada, E.; Island, J. O.; Narasimha-Acharya, K. L.; Blanter, S. I.; Groenendijk, D. J.; Buscema, M.; Steele, G. A.; Alvarez, J. V.; Zandbergen, H. W.; Palacios, J. J.; Van Der Zant, H. S. J. Isolation and Characterization of Few-Layer Black Phosphorus. *2D Mater.* **2014**, 1, 25001.

[22] Pang, S.-Y.; Wong, Y.-T.; Yuan, S.; Liu, Y.; Tsang, M.-K.; Yang, Z.; Huang, H.; Wong, W.-T.; Hao, J. Universal Strategy for HF-Free Facile and Rapid Synthesis of Two-Dimensional Mxenes as Multifunctional Energy Materials. *J. Am. Chem. Soc.* **2019**, 141, 9610-9616.

[23] Pang, S. Y.; Io, W. F.; Wong, L. W.; Zhao, J.; Hao, J. Efficient Energy Conversion and Storage Based on Robust Fluoride-Free Self-Assembled 1D Niobium Carbide in 3D Nanowire Network. *Adv. Sci.* **2020**, 7, 1903680.

[24] Mannix, A. J.; Kiraly, B.; Hersam, M. C.; Guisinger, N. P. Synthesis and Chemistry of Elemental 2D Materials. *Nat. Rev. Chem.* **2017**, 1.

[25] Campbell, M. G.; Liu, S. F.; Swager, T. M.; Dincă, M. Chemiresistive Sensor Arrays from Conductive 2D Metal–Organic Frameworks. *J. Am. Chem. Soc.*

2015, 137, 13780-13783.

[26] Zhao, M.; Wang, Y.; Ma, Q.; Huang, Y.; Zhang, X.; Ping, J.; Zhang, Z.; Lu, Q.; Yu, Y.; Xu, H.; Zhao, Y.; Zhang, H. Ultrathin 2D Metal–Organic Framework Nanosheets. *Adv. Mater.* **2015**, 27, 7372-7378.

[27] Kandambeth, S.; Mallick, A.; Lukose, B.; Mane, M. V.; Heine, T.; Banerjee, R. Construction of Crystalline 2D Covalent Organic Frameworks with Remarkable Chemical (Acid/Base) Stability via a Combined Reversible and Irreversible Route. *J. Am. Chem. Soc.* **2012**, 134, 19524-19527.

[28] Côté, A. P.; El-Kaderi, H. M.; Furukawa, H.; Hunt, J. R.; Yaghi, O. M. Reticular Synthesis of Microporous and Mesoporous 2D Covalent Organic Frameworks. *J. Am. Chem. Soc.* **2007**, 129, 12914-12915.

[29] Yu, J.; Li, J.; Zhang, W.; Chang, H. Synthesis of High Quality Two-Dimensional Materials via Chemical Vapor Deposition. *Chem. Sci.* **2015**, 6, 675-6716.

[30] Jonathan, N. C.; Mustafa, L.; Arlene, O.; apos; Neill; Shane, D. B.; Paul, J. K.; Umar, K.; Karen, Y.; Alexandre, G.; Sukanta, D.; Ronan, J. S.; Igor, V. S.; Sunil, K. A.; George, S.; Hye-Young, K.; Kangho, L.; Gyu Tae, K.; Georg, S. D.; Toby, H.; John, J. B.; Jing Jing, W.; John, F. D.; Jaime, C. G.; Gregory, M.; Aleksey, S.; Rebecca, J. N.; James, M. P.; Eleanor, M. G.; Koenraad, T.; David, W. M.; Peter, D. N.; Valeria, N. Two-Dimensional Nanosheets Produced by Liquid Exfoliation of Layered Materials. *Science* **2011**, 331, 568-571.

[31] Yang, Z.; Hao, J. Recent Progress in 2D Layered III–VI Semiconductors and their Heterostructures for Optoelectronic Device Applications. *Adv. Mater. Technol.* **2019**, 4, 1900108.

[32] Zhang, H. Ultrathin Two-Dimensional Nanomaterials. *ACS Nano* **2015**, 9, 9451-9469.

[33] Novoselov, K.; Mishchenko, A.; Carvalho, A.; Neto, A. C. 2D Materials and van der Waals Heterostructures. *Science* **2016**, 353, aac9439.

[34] Geim, A. K.; Grigorieva, I. V. Van der Waals Heterostructures. *Nature* **2013**, 499, 419-425.

[35] Liang, S.-J.; Cheng, B.; Cui, X.; Miao, F. Van der Waals Heterostructures for High-Performance Device Applications: Challenges and Opportunities. *Adv. Mater.* **2019**, e1903800.

[36] Georgiou, T.; Jalil, R.; Belle, B. D.; Britnell, L.; Gorbachev, R. V.; Morozov, S. V.; Kim, Y.-J.; Gholinia, A.; Haigh, S. J.; Makarovsky, O. Vertical Field-Effect Transistor Based on Graphene–WS_2 Heterostructures for Flexible and Transparent Electronics. *Nat. Nanotech.* **2013**, 8, 100-103.

[37] Tongay, S.; Fan, W.; Kang, J.; Park, J.; Koldemir, U.; Suh, J.; Narang, D. S.; Liu,

K.; Ji, J.; Li, J. Tuning Interlayer Coupling In Large-Area Heterostructures With CVD-Grown MoS_2 and WS_2 monolayers. *Nano Lett.* **2014**, 14, 3185-3190.

[38] Wei, P.; Lee, S.; Lemaitre, F.; Pinel, L.; Cutaia, D.; Cha, W.; Katmis, F.; Zhu, Y.; Heiman, D.; Hone, J. Strong Interfacial Exchange Field in the Graphene/Eus Heterostructure. *Nat. Mater.* **2016**, 15, 711-716.

[39] Dean, C. R.; Young, A. F.; Meric, I.; Lee, C.; Wang, L.; Sorgenfrei, S.; Watanabe, K.; Taniguchi, T.; Kim, P.; Shepard, K. L. J. N. n. Boron Nitride Substrates for High-Quality Graphene Electronics. *Nat. Nanotech.* **2010**, 5, 722-726.

[40] Gong, Y.; Lei, S.; Ye, G.; Li, B.; He, Y.; Keyshar, K.; Zhang, X.; Wang, Q.; Lou, J.; Liu, Z. J. N. l. Two-Step Growth of Two-Dimensional WSe_2/$MoSe_2$ Heterostructures. *Nano Lett.* **2015**, 15, 6135-6141.

[41] He, J.; Li, T.; Zhang, L.; He, D.; Wang, Y.; Ding, H.; Pan, N.; Zhao, H. Efficient Energy Transfer in In_2Se_3–$MoSe_2$ van der Waals Heterostructures. *ACS omega* **2018**, 3, 11930-11936.

[42] Gong, Y.; Lin, J.; Wang, X.; Shi, G.; Lei, S.; Lin, Z.; Zou, X.; Ye, G.; Vajtai, R.; Yakobson, B. I.; Terrones, H.; Mauricio Terrones; Beng Kang Tay; Jun Lou, S. T. P.; Liu, Z.; Zhou, W.; M., A. P. Vertical and In-Plane Heterostructures from WS_2/ MoS_2 Monolayers. *Nat. Mater.* **2014**, 13, 1135-1142.

[43] Han, G. H.; Rodríguez-Manzo, J. A.; Lee, C.-W.; Kybert, N. J.; Lerner, M. B.; Qi, Z. J.; Dattoli, E. N.; Rappe, A. M.; Drndic, M.; Johnson, A. C. Continuous Growth of Hexagonal Graphene and Boron Nitride In-Plane Heterostructures by Atmospheric Pressure Chemical Vapor Deposition. *Acs Nano* **2013**, 7, 10129-10138.

[44] Zheng, F.; Xin, Y.; Huang, W.; Zhang, J.; Wang, X.; Shen, M.; Dong, W.; Fang, L.; Bai, Y.; Shen, X.; Hao, J. Above 1% Efficiency of a Ferroelectric Solar Cell Based on the $Pb(Zr, Ti)O_3$ Film. *J. Mater. Chem. A* **2014**, 2, 1363-1368.

[45] Zhang, Y.; Jie, W.; Chen, P.; Liu, W.; Hao, J. Ferroelectric and Piezoelectric Effects on the Optical Process in Advanced Materials and Devices. *Adv. Mater.* **2018**, 30, 1707007.

[46] Yuan, S.; Yang, Z.; Xie, C.; Yan, F.; Dai, J.; Lau, S. P.; Chan, H. L.; Hao, J. Ferroelectric-Driven Performance Enhancement of Graphene Field-Effect Transistors Based on Vertical Tunneling Heterostructures. *Adv. Mater.* **2016**, 28, 10048-10054.

[47] Jeong, D. S.; Thomas, R.; Katiyar, R.; Scott, J.; Kohlstedt, H.; Petraru, A.; Hwang, C. S. Emerging Memories: Resistive Switching Mechanisms and Current Status. *Rep. Prog. Phys.* **2012**, 75, 076502.

[48] Valasek, J. Piezo-electric and Allied Phenomena in Rochelle Salt. *Phys. Rev.*

1921, 17, 475.

[49] Grinberg, I.; West, D. V.; Torres, M.; Gou, G.; Stein, D. M.; Wu, L.; Chen, G.; Gallo, E. M.; Akbashev, A. R.; Davies, P. K.; Spanier, J. E.; Rappe, A. M. Perovskite Oxides for Visible-Light-Absorbing Ferroelectric and Photovoltaic Materials. *Nature* **2013**, 503, 509-512.

[50] Dawber, M.; Rabe, K. M.; Scott, J. F. Physics of Thin-Film Ferroelectric Oxides. *Rev. Mod. Phys.* **2005**, 77, 1083-1130.

[51] Wang, Y.; Chen, W.; Wang, B.; Zheng, Y. Ultrathin Ferroelectric Films: Growth, Characterization, Physics and Applications. *Materials* **2014**, 7, 6377-6485.

[52] Scott, J. F. Applications of Modern Ferroelectrics. *Science* **2007**, 315, 954-959.

[53] Yuan, Y.; Xiao, Z.; Yang, B.; Huang, J. Arising Applications of Ferroelectric Materials in Photovoltaic Devices. *J. Mater. Chem. A* **2014**, 2, 6027-6041.

[54] Li, M.; Pietrowski, M. J.; De Souza, R. A.; Zhang, H.; Reaney, I. M.; Cook, S. N.; Kilner, J. A.; Sinclair, D. C. A Family of Oxide Ion Conductors Based on the Ferroelectric Perovskite $Na_{0.5}Bi_{0.5}TiO_3$. *Nat. Mater.* **2014**, 13, 31-35.

[55] Junquera, J.; Ghosez, P. Critical Thickness for Ferroelectricity in Perovskite Ultrathin Films. *Nature materials* **2003**, 422, 506-509.

[56] Sai, N.; Kolpak, A. M.; Rappe, A. M. Ferroelectricity in Ultrathin Perovskite Films. *Phys. Rev. B* **2005**, 72, 020101.

[57] Gao, P.; Zhang, Z.; Li, M.; Ishikawa, R.; Feng, B.; Liu, H.-J.; Huang, Y.-L.; Shibata, N.; Ma, X.; Chen, S. J. N. c. Possible Absence of Critical Thickness and Size Effect in Ultrathin Perovskite Ferroelectric Films. *Nat. Commun.* **2017**, 8, 1-8.

[58] Lee, D.; Lu, H.; Gu, Y.; Choi, S.-Y.; Li, S.-D.; Ryu, S.; Paudel, T.; Song, K.; Mikheev, E.; Lee, S. J. S. Emergence of Room-Temperature Ferroelectricity at Reduced Dimensions. *Science* **2015**, 349, 1314-1317.

[59] Fong, D. D.; Stephenson, G. B.; Streiffer, S. K.; Eastman, J. A.; Auciello, O.; Fuoss, P. H.; Thompson, C. Ferroelectricity in Ultrathin perovskite films. *Science* **2004**, 304, 1650-1653.

[60] Gerra, G.; Tagantsev, A.; Setter, N.; Parlinski, K. J. P. r. l. Ionic Polarizability of Conductive Metal Oxides And Critical Thickness for Ferroelectricity in $BaTiO_3$. *Physl Rev. Lett.* **2006**, 96, 107603.

[61] Tsvetkov, N.; Lu, Q.; Sun, L.; Crumlin, E. J.; Yildiz, B. Improved Chemical and Electrochemical Stability of Perovskite Oxides with Less Reducible Cations at the Surface. *Nat. Mater.* **2016**, 15, 1010-1016.

[62] Scott, J. F.; Dawber, M. Oxygen-Vacancy Ordering as a Fatigue Mechanism in Perovskite Ferroelectrics. *Appl. Phys. Lett.* **2000**, 76, 3801-3803.

[63] Park, M. H.; Lee, Y. H.; Kim, H. J.; Kim, Y. J.; Moon, T.; Kim, K. D.; Müller, J.; Kersch, A.; Schroeder, U.; Mikolajick, T.; Hwang, C. S. Ferroelectricity and Antiferroelectricity of Doped Thin HfO_2-Based Films. *Adv. Mater.* **2015**, 27, 1811-1831.

[64] Müller, J.; Böscke, T. S.; Schröder, U.; Mueller, S.; Bräuhaus, D.; Böttger, U.; Frey, L.; Mikolajick, T. Ferroelectricity in Simple Binary ZrO_2 and HfO_2. *Nano. Lett.* **2012**, 12, 4318-4323.

[65] Mueller, S.; Mueller, J.; Singh, A.; Riedel, S.; Sundqvist, J.; Schroeder, U.; Mikolajick, T. Incipient Ferroelectricity in Al-Doped HfO_2 Thin Films. *Adv. Funct. Mater.* **2012**, 22, 2412-2417.

[66] Böscke, T.; Müller, J.; Bräuhaus, D.; Schröder, U.; Böttger, U. Ferroelectricity in Hafnium Oxide Thin Films. *Appli. Phys. Lett* **2011**, 99, 102903.

[67] Cheema, S. S.; Kwon, D.; Shanker, N.; Dos Reis, R.; Hsu, S.-L.; Xiao, J.; Zhang, H.; Wagner, R.; Datar, A.; McCarter, M. Enhanced Ferroelectricity in Ultrathin Films Grown Directly on Silicon. *Nat. Mater.* **2020**, 580, 478-482.

[68] Cui, C.; Xue, F.; Hu, W.-J.; Li, L.-J. Two-Dimensional Materials with Piezoelectric and Ferroelectric Functionalities. *npj 2D Mater. Appl.* **2018**, 2, 1-14.

[69] Wu, W.; Wang, L.; Li, Y.; Zhang, F.; Lin, L.; Niu, S.; Chenet, D.; Zhang, X.; Hao, Y.; Heinz, T. F.; Hone, J.; Wang, Z. L. Piezoelectricity of Single-Atomic-Layer MoS_2 for Energy Conversion and Piezotronics. *Nature* **2014**, 514, 470-474.

[70] Meyer, J. C.; Geim, A. K.; Katsnelson, M. I.; Novoselov, K. S.; Booth, T. J.; Roth, S. The Structure of Suspended Graphene Sheets. *Nature* **2007**, 446, 60-63.

[71] Fei, R.; Kang, W.; Yang, L. Ferroelectricity and Phase Transitions in Monolayer Group-IV Monochalcogenides. *Phys. Rev. Lett.* **2016**, 117, 097601.

[72] Xiao, C.; Wang, F.; Yang, S. A.; Lu, Y.; Feng, Y.; Zhang, S. Elemental Ferroelectricity and Antiferroelectricity in Group-V Monolayer. *Adv. Functi. Mater.* **2018**, 28, 1707383-n/a.

[73] Shirodkar, S. N.; Waghmare, U. V. Emergence of Ferroelectricity at a Metal-Semiconductor Transition in a 1T Monolayer of MoS_2. *Phys. Rev. Lett.* **2014**, 112, 157601.

[74] Xu, B.; Xiang, H.; Xia, Y.; Jiang, K.; Wan, X.; He, J.; Yin, J.; Liu, Z. Monolayer $AgBiP_2Se_6$: an Atomically Thin Ferroelectric Semiconductor with Out-Plane Polarization. *Nanoscale* **2017**, 9, 8427-8434.

[75] Reimers, J. R.; Tawfik, S. A.; Ford, M. J. J. C. s. Van der Waals Forces Control

Ferroelectric–Antiferroelectric Ordering in $CuInP_2S_6$ And $CuBiP_2S_6$ Laminar Materials. *Chem. Sci.* **2018**, 9, 7620-7627.

[76] Ding, W.; Zhu, J.; Wang, Z.; Gao, Y.; Xiao, D.; Gu, Y.; Zhang, Z.; Zhu, W. Prediction of Intrinsic Two-Dimensional Ferroelectrics in In_2Se_3 and Other III_2-VI_3 van der Waals Materials. *Nature Communications* **2017**, 8, 14956.

[77] Chang, K.; Liu, J.; Lin, H.; Wang, N.; Zhao, K.; Zhang, A.; Jin, F.; Zhong, Y.; Hu, X.; Duan, W.; ZhangQingming; Liang, F.; Qi-Kun, X.; Xi, C.; Shuai-Hua, J. Discovery of Robust In-Plane Ferroelectricity in Atomic-Thick SnTe. *Science* **2016**, 353, 274-278.

[78] Zheng, C.; Yu, L.; Zhu, L.; Collins, J. L.; Kim, D.; Lou, Y.; Xu, C.; Li, M.; Wei, Z.; Zhang, Y.; Edmonds, M. T.; Li, S.; Seidel, J.; Zhu, Y.; Liu, Z. J.; Tang, W.-X.; Fuhrer, M. S. Room Temperature In-Plane Ferroelectricity in van der Waals In_2Se_3. *Sci. Adv.* **2018**, 4.

[79] You, L.; Liu, F.; Li, H.; Hu, Y.; Zhou, S.; Chang, L.; Zhou, Y.; Fu, Q.; Yuan, G.; Dong, S.; Fan, H. J.; Gruverman, A.; Liu, Z.; Wang, J. In-Plane Ferroelectricity in Thin Flakes of Van der Waals Hybrid Perovskite. *Adv. Mater.* **2018**, 30, e1803249-n/a.

[80] Higashitarumizu, N.; Kawamoto, H.; Lee, C.-J.; Lin, B.-H.; Chu, F.-H.; Yonemori, I.; Nishimura, T.; Wakabayashi, K.; Chang, W.-H.; Nagashio, K. Purely In-Plane Ferroelectricity in Monolayer SnS at Room Temperature. *Nat. Commun.* **2020**, 11, 1-9.

[81] Belianinov, A.; He, Q.; Dziaugys, A.; Maksymovych, P.; Eliseev, E.; Borisevich, A.; Morozovska, A.; Banys, J.; Vysochanskii, Y.; Kalinin, S. V. $CuInP_2S_6$ Room Temperature Layered Ferroelectric. *Nano Lett.* **2015**, 15, 3808-3814.

[82] Fei, Z.; Zhao, W.; Palomaki, T. A.; Sun, B.; Miller, M. K.; Zhao, Z.; Yan, J.; Xu, X.; Cobden, D. H. Ferroelectric Switching of a Two-Dimensional Metal. *Nature* **2018**, 560, 336-339.

[83] Yuan, S.; Luo, X.; Chan, H. L.; Xiao, C.; Dai, Y.; Xie, M.; Hao, J. Room-Temperature Ferroelectricity in $MoTe_2$ Down to the Atomic Monolayer Limit. *Nat. Commun.* **2019**, 10, 1-6.

[84] Xiao, J.; Zhu, H.; Wang, Y.; Feng, W.; Hu, Y.; Dasgupta, A.; Han, Y.; Wang, Y.; Muller, D. A.; Martin, L. W.; Hu, P.; Zhang, X. Intrinsic Two-Dimensional Ferroelectricity with Dipole Locking. *Phys. Rev. Lett.* **2018**, 120, 227601.

[85] Xue, F.; Hu, W.; Lee, K. C.; Lu, L. S.; Zhang, J.; Tang, H. L.; Han, A.; Hsu, W. T.; Tu, S.; Chang, W. H.; Lien, C. H.; He, J. H.; Zhang, Z.; Li, L. J.; Zhang, X. Room-Temperature Ferroelectricity in Hexagonally Layered α-In_2Se_3 Nanoflakes down to the Monolayer Limit. *Adv. Funct. Mater.* **2018**, 28, n/a.

[86] Liu, F.; You, L.; Seyler, K. L.; Li, X.; Yu, P.; Lin, J.; Wang, X.; Zhou, J.; Wang, H.; He, H. Room-Temperature Ferroelectricity in $CuInP_2S_6$ Ultrathin Flakes. *Nat. Commun.* **2016**, 7, 1-6.

[87] Lai, Y.; Song, Z.; Wan, Y.; Xue, M.; Wang, C.; Ye, Y.; Dai, L.; Zhang, Z.; Yang, W.; Du, H. Two-Dimensional Ferromagnetism and Driven Ferroelectricity in van der Waals $CuCrP_2S_6$. *Nanoscale* **2019**, 11, 5163-5170.

[88] Wang, X.-Y.; Narita, A.; Müllen, K. Precision Synthesis versus Bulk-Scale Fabrication of Graphenes

Nat. Rev. Chem. **2017**, 2, 1-10.

[89] Chen, W.; Wang, J.; Wan, F.; Wang, P. Review of Optical Fibre Sensors for Electrical Equipment Characteristic State Parameters Detection. *High Volt.* **2019**, 4, 271-281.

[90] EDX Analysis with a Scanning Electron Microscope (SEM): How Does It Work? *Thermo Fisher Scientific*. [Online]. Available: https://www.thermofisher.com/hk/en/home/global/forms/industrial/edx-analysis-sem.html

[91] V., B. P.; Dezhen, X.; Turab, L. Structure–Curie Temperature Relationships in $BaTiO_3$-Based Ferroelectric Perovskites: Anomalous Behavior of $(Ba, Cd) TiO_3$ from DFT, Statistical Inference, and Experiments. *Phys. Rev. B* **2016**, 93, 144111.

[92] Lang, X.; Jiang, Q. Size and Interface Effects on Curie Temperature of Perovskite Ferroelectric Nanosolids. *Nanoparticle Res.* **2007**, 9, 595-603.

[93] Liu, C.; Wan, W.; Ma, J.; Guo, W.; Yao, Y. Robust Ferroelectricity in Two-Dimensional SbN and BiP. *Nanoscale* **2018**, 10, 7984-7990.

[94] Chandrasekaran, A.; Mishra, A.; Singh, A. K. Ferroelectricity, Antiferroelectricity, and Ultrathin 2D Electron/Hole Gas in Multifunctional Monolayer MXene. *Nano Lett.* **2017**, 17, 3290-3296.

[95] Cui, C.; Hu, W.-J.; Yan, X.; Addiego, C.; Gao, W.; Wang, Y.; Wang, Z.; Li, L.; Cheng, Y.; Li, P.; Zhang, X.; Alshareef, H. N.; Wu, T.; Zhu, W.; Pan, X.; Li, L.-J. Intercorrelated In-Plane and Out-of-Plane Ferroelectricity in Ultrathin Two-Dimensional Layered Semiconductor In_2Se_3. *Nano Lett.* **2018**, 18, 1253-1258.

[96] Poh, S. M.; Tan, S. J. R.; Wang, H.; Song, P.; Abidi, I. H.; Zhao, X.; Dan, J.; Chen, J.; Luo, Z.; Pennycook, S. J.; Castro Neto, A. H.; Loh, K. P. Molecular-Beam Epitaxy of Two-Dimensional In_2Se_3 and Its Giant Electroresistance Switching in Ferroresistive Memory Junction. *Nano Lett.* **2018**, 18, 6340-6346.

[97] Zhou, Y.; Wu, D.; Zhu, Y.; Cho, Y.; He, Q.; Yang, X.; Herrera, K.; Chu, Z.; Han, Y.; Downer, M. C.; Peng, H.; Lai, K. Out-of-Plane Piezoelectricity and

Ferroelectricity in Layered α-In_2Se_3 Nanoflakes. *Nano Lett.* **2017**, 17, 5508-5513.

[98] Wan, S.; Li, Y.; Li, W.; Mao, X.; Wang, C.; Chen, C.; Dong, J.; Nie, A.; Xiang, J.; Liu, Z.; Zhu, W.; Zeng, H. Nonvolatile Ferroelectric Memory Effect in Ultrathin α-In_2Se_3. *Adv. Funct. Mater.* **2019**, 29, n/a.

[99] Wan, S.; Li, Y.; Li, W.; Mao, X.; Zhu, W.; Zeng, H. Room-Temperature Ferroelectricity and a Switchable Diode Effect in Two-Dimensional α-In_2Se_3 Thin Layers. *Nanoscale* **2018**, 10, 14885-14892.

[100] Vysochanskii, Y. M.; Stephanovich, V.; Molnar, A.; Cajipe, V.; Bourdon, X. Raman Spectroscopy Study of the Ferrielectric-Paraelectric Transition in Layered $CuInP_2S_6$. *Phys. Rev. B* **1998**, 58, 9119.

[101] Jasinski, J.; Swider, W.; Washburn, J.; Liliental-Weber, Z.; Chaiken, A.; Nauka, K.; Gibson, G. A.; Yang, C. C. Crystal structure of kappa-In2Se3. **2002**.

[102] Jacobs-Gedrim, R. B.; Shanmugam, M.; Jain, N.; Durcan, C. A.; Murphy, M. T.; Murray, T. M.; Matyi, R. J.; Moore, R. L.; Yu, B. Extraordinary Photoresponse in Two-Dimensional In_2Se_3 Nanosheets. *ACS Nano* **2014**, 8, 514-521.

[103] Jo, J. Y.; Kim, Y. S.; Noh, T. W.; Yoon, J.-G.; Song, T. K. Coercive Fields in Ultrathin $BaTiO_3$ Capacitors. *Appl. Phys. Lett.* **2006**, 89, 232909.

[104] Dawber, M.; Chandra, P.; Littlewood, P. B.; Scott, J. F. Depolarization Corrections to the Coercive Field in Thin-Film Ferroelectrics. *J. Phys.: Condens. Matter* **2003**, 15, L393.

[105] Ducharme, S.; Fridkin, V. M.; Bune, A. V.; Palto, S. P.; Blinov, L. M.; Petukhova, N. N.; Yudin, S. G. Intrinsic Ferroelectric Coercive Field. *Phys. Rev. Lett.* **2000**, 84, 175-177.

[106] Luo, J.; Sun, W.; Zhou, Z.; Bai, Y.; Wang, Z. J.; Tian, G.; Chen, D.; Gao, X.; Zhu, F.; Li, J.-F. Domain Evolution and Piezoelectric Response across Thermotropic Phase Boundary in (K,Na)NbO_3-Based Epitaxial Thin Films. *ACS Appl. Mater. Interfaces* **2017**, 9, 13315-13322.

[107] Zhang, X.; Xu, H.; Zhang, Y. Temperature Dependence of Coercive Field and Fatigue In Poly(Vinylidene Fluoride-Trifluoroethylene) Copolymer Ultra-Thin Films. *J. Phys. D: Appl. Phys.* **2011**, 44, 155501.

[108] Qiao, H.; He, C.; Wang, Z.; Pang, D.; Li, X.; Liu, Y.; Long, X. Influence of Mn Dopants on the Electrical Properties of $Pb(In_{0.5}Nb_{0.5})O_3$-$PbTiO_3$ Ferroelectric Single Crystals. *RSC Adv.* **2017**, 7, 32607-32612.

[109] Tao, X.; Gu, Y. Crystalline–Crystalline Phase Transformation in Two-Dimensional In_2Se_3 Thin Layers. *Nano Lett.* **2013**, 13, 3501-3505.

[110] Liu, J.; Pantelides, S. T. Pyroelectric Response and Temperature-Induced α -β

Phase Transitions in α-In_2Se_3 and Other α-III_2VI_3 (III = Al, Ga, In VI = S, Se) Monolayers. *2D Mater.* **2019**, 6, 25001.

[111] Ho, C.-H. Amorphous Effect on the Advancing of Wide-Range Absorption and Structural-Phase Transitionin γ-In_2Se_3 Polycrystalline Layers. *Sci. Rep.* **2014**, 4, 4764.

[112] Almahmoud, E.; Kornev, I.; Bellaiche, L. Dependence of Curie Temperature on the Thickness of an Ultrathin Ferroelectric Film. *Phys. Rev. B Condens. Matter Mater. Phys.* **2010**, 81, 064105.

[113] Ishikawa, K.; Nomura, T.; Okada, N.; Takada, K. Size Effect on the Phase Transition in $PbTiO_3$ Fine Particles. *Jpn. J. Appl. Phys.* **1996**, 35, 5196-5198.

[114] Mbarki, R.; Haskins, J. B.; Kinaci, A.; Cagin, T. Temperature Dependence of Flexoelectricity in $BaTiO_3$ and $SrTiO_3$ Perovskite Nanostructures *Phys. Lett. A* **2014**, 378, 2181-2183.

[115] Liu, B.; Tang, B.; Lv, F.; Zeng, Y.; Liao, J.; Wang, S.; Chen, Q. Photodetector Based on Heterostructure of Two-dimensional WSe_2/In_2Se_3. *Nanotechnology* **2020**, 31, 65203-065203.

[116] Vysochanskii, Y. Ferroelectricity in Complex Chalcogenides $M'M''P_2X_6$ (M′, M″-Sn, Pb, Cu, In, Cr; X-S, Se). *Ferroelectrics* **1998**, 218, 275-282.

[117] Si, M.; Liao, P.-Y.; Qiu, G.; Duan, Y.; Ye, P. D. Ferroelectric Field-Effect Transistors Based on MoS_2 and $CuInP_2S_6$ Two-Dimensional van der Waals Heterostructure. *Acs Nano* **2018**, 12, 6700-6705.